TITLE: "A dynamic *in vitro* model of Down Syndrome neurogenesis with Trisomy 21 gene dosage correction"

Prakhar Bansal [1,2,7], Erin. C Banda [2,7], Heather R. Glatt-Deeley [2], Christopher E. Stoddard [3], Darcy T. Ahern [1,2], Yuvabharath Kondaveeti [2,4], Michael Nicouleau [5] and Stefan F. Pinter [1,2,6 *]

[1] Graduate Program in Genetics and Developmental Biology, UCONN Health, University of Connecticut, Farmington, CT, United States

[2] Department of Genetics and Genome Sciences, UCONN Health, University of Connecticut, Farmington, CT, United States

[3] Cell and Genome Engineering Core, UCONN Health, University of Connecticut, Farmington, CT, United States

[4] Current: Enzerna Biosciences, Morrisville, NC

[5] Current: Early Drug Discovery Unit, Montreal Neurology Institute, McGill University

[6] Institute for Systems Genomics, University of Connecticut, Farmington, CT, United States

[7] These authors contributed equally

[*] Corresponding author: spinter@uchc.edu

ABSTRACT/SUMMARY

Excess gene dosage from human chromosome 21 (HSA21), due to trisomy or translocation of HSA21 material, causes Down syndrome (DS). Trisomy 21 (T21) results in a large number of developmental and ongoing cellular phenotypes, raising the critical question of whether some of the latter may remain amenable to intervention after development. To generate an *in vitro* model of DS neurogenesis with dynamic T21 dosage, we derived T21 human induced pluripotent stem cells (hiPSCs) alongside otherwise isogenic euploid controls from mosaic DS fibroblasts, and equipped one distinct HSA21 copy with a new inducible *XIST* transgene. Phased genotyping enables us to apply this unique biological resource to allelic transcriptome analyses that demonstrate that T21 silencing by *XIST* is largely complete and irreversible in hiPSCs. Differential expression analysis reveals T21 neural lineages and hiPSCs share suppressed translation and mitochondrial pathways, and activate cellular stress responses. When *XIST* is induced prior to the neural progenitor stage, T21 dosage correction suppresses a pronounced skew towards excessive astrogenesis in T21 neural differentiation. Because our *XIST* transgene remains inducible in post-mitotic T21 neurons and astrocytes, this dynamic model of HSA21 gene dosage will empower systematic exploration of cellular and transcriptional T21 phenotypes that depend on acute T21 gene dosage in differentiated cell types.

KEYWORDS:

59 **INTRODUCTION**

60 Down syndrome (DS), the most prevalent human viable aneuploidy (trisomy 21, T21 in up to
61 1:700 live births) poses three significant challenges to understanding and addressing the clinical
62 needs of people living with DS [1]. First, our understanding of the developmental etiology
63 underlying cardiac, hematopoietic and neurological defects in DS is still limited [2]. Ever-more
64 sophisticated rodent DS models faithfully carry most of human chromosome 21 (HSA21) [3] or
65 traverse syntenic boundaries to represent supernumerary mouse HSA21 orthologs [4]. While these
66 rodent models capture many important aspects of DS, human trisomy 21 (T21) induced
67 pluripotent stem cells (hiPSCs) are increasingly serving as an important complementary model
68 for DS development and pre-clinical research [5]. These hiPSC models may prove especially relevant
69 to human-specific aspects of development, for example by reflecting brain region-specific neural
70 cell types [6] and intrinsically extended human neuronal maturation [7].

71 Second, there is lack of approaches to systematically distinguish irreversible developmental
72 phenotypes from "acute" cellular phenotypes that may remain amenable to postnatal
73 intervention. Because supernumerary HSA21 genes or their rodent orthologs are present
74 throughout differentiation or development of such DS hiPSC and rodent DS models, respectively,
75 we have an incomplete view of which cellular DS phenotypes depend on ongoing excess HSA21
76 dosage in terminally differentiated cells. This questions is particularly relevant to DS-associated
77 neurodegeneration [8].

78 Third, cellular stress pathways that are chronically and systemically active in DS [9–14] and likely
79 play an important role in DS neurodegeneration [15], are also shared with human trisomies 13 (T13)
80 and 18 (T18) [16], but not with dosage-compensated sex-chromosomal trisomy. The most plausible
81 origin for such common aneuploidy-associated cellular stress is that it results from compound
82 excess expression of the many autosomal genes that code for subunits of dosage-sensitive
83 protein complexes. However, this interpretation has not yet been tested formally in the context
84 of an autosomal trisomy, as it requires distinguishing excess expression from the mere presence
85 of the supernumerary chromosome.

86 A human cellular model with dynamic T21 gene dosage could be instrumental towards
87 addressing these challenges, across a range of DS-affected cell fates and phenotypes. To

88 characterize the impact of T21 in hiPSCs and terminally differentiated cell types, we generated
89 such a dynamic hiPSC model of T21 dosage alongside otherwise isogenic controls from mosaic
90 DS. Pioneering work by the Lawrence lab demonstrated the utility of the long non-coding RNA
91 *XIST*, which endogenously silences the inactive X in females, for T21 dosage correction in DS
92 hiPSCs [17,18]. *XIST* RNA spreads from its site of transcription across the entire chromosome *in cis*,
93 to directly and indirectly recruit orthogonal repressive chromatin complexes to silence genes [19].
94 Earlier work in the mouse system indicated that *Xist* could establish gene silencing only when
95 during or upon exiting pluripotency, but not after differentiation [20,21], with rare exception [22,23].
96 Recent work by the Lawrence lab shows that human *XIST* can still silence genes up to the neural
97 progenitor cell (NPC) stage, but technical limitations hindered *XIST* induction in terminal, post-
98 mitotic human neural cells [24]. Another system induced *XIST* in human T21 astroglial progenitors
99 via high expression of the doxycycline (dox)-responsive reverse tet-trans-activator (rtTA) re-
100 delivered at the NPC stage, but only achieved partial T21 repression [25].
101 Here, we leverage phased allelic expression analysis to demonstrate that our new inducible
102 T21-*XIST* design enables uniform, near-complete -and irreversible T21 dosage correction in
103 hiPSCs, and remains inducible in terminal neural cell fates. *XIST* suppresses T21 *trans*-effects,
104 including cellular stress pathways that are also active in T21 neural lineages. T21 silencing prior
105 to the neural progenitor cell (NPC) stage rescues T21-altered neuro-astroglial lineage balance
106 that reflects excess gliogenesis previously observed in DS fetal samples [26–30] and rodent models
107 [31–35]. Because our T21-*XIST* system is also the first to effectively induce *XIST* in post-mitotic
108 neurons and astrocytes, this model of dynamic T21 gene dosage will facilitate identification of
109 cellular pathways that may present promising targets for intervention after completed
110 development.
111
112 **RESULTS**
113 To derive T21 hiPSCs alongside isogenic euploid control lines, we reprogrammed dermal
114 fibroblasts from a male individual with mosaic DS [36], and screened the resulting hiPSC clones
115 using copy-number sensitive qPCR [Fig. S1A,B]. Two T21 lines appeared to have a gain on HSA17,
116 a frequent karyotypic abnormality primarily observed in human ESCs [37,38], but featured only two

117 centromere 17 signals by fluorescent *in-situ* hybridization (FISH) follow-up [Fig. S1C]. We
118 performed array comparative genomic hybridization (aCGH, CytoSNP-850k) to confirm expected
119 karyotypes for fibroblasts, euploid and T21 hiPSCs, and to resolve segmental (17q) gains in the
120 two corresponding clones, which were excluded thereafter [Fig. S1D]. Differential probe intensity
121 analysis of the remaining T21 and euploid hiPSC lines also revealed a large set of heterozygous
122 SNPs with increased representation in the euploid lines spanning HSA21, and a smaller focal set
123 that was lost in euploid lines [Fig. S1E]. These results suggested one HSA21 copy from each parent
124 was maintained in euploid lines (M & P), whereas T21 hiPSCs carried an additional copy (M2), in
125 likely a maternal chromatid retained via non-disjunction in meiosis II [39].

126 While T21 is stably maintained in hiPSCs after reprogramming [40–42], sporadic T21 loss has
127 been reported [43,44]. We therefore confirmed the mitotic stability of three HSA21 copies by two
128 independent approaches. First, three independent signals are observed in 94.5% of T21 hiPSCs
129 by fluorescent *in-situ* hybridization (FISH, *DSCR8* probe), compared to 99% of euploid hiPSCs with
130 two signals [Fig. S1F]. Second, while targeting a *UBC*-promoter driven doxycycline (dox)-
131 responsive trans-activator (rTTA3G) to the AAVS1 safe harbor in *PPP1R12C* (HSA19), we
132 confirmed that all 32/32 independent colonies arising from single cells maintained T21 by copy-
133 number sensitive qPCR for a *DYRK1A* amplicon [Fig. S1G].

134 We integrated our TET3G-driven *XIST* cDNA transgene on HSA21^{P} [Fig. 1A], after re-
135 verifying the karyotypic integrity of rTTA3G clones by aCGH [Fig. S1D]. To this end, we designed
136 Cas9 guides dependent on a HSA21^{P}-specific protospacer adjacent motif (PAM), targeting an
137 intergenic site well outside of *DYRK1A* to avoid impacting its expression. We proceeded with
138 three independent, PCR-screened T21-*XIST* clones, and tested the efficacy of *XIST* induction by
139 RNA-FISH and immuno-fluorescence (IF) staining. Ubiquitinated histone 2A lysine 119
140 (H2AK119ub) and tri-methylated histone 3 lysine 27 (H3K27me3) follow *XIST/Xist* RNA expression
141 on mouse and human X alike [19]. Of note, because the original fibroblasts were from a male
142 individual with DS, there is only a single X in these hiPSCs [Fig. S1C], and any *XIST*,
143 H2A119ub/H3K27me3 clouds arise from the T21-targeted *XIST* transgene. Indeed, hiPSCs without
144 acute dox treatment (3 wk withdrawal, w/d) are negative for XIST, underscoring the TET3G
145 system is not leaky and turns off when dox is withdrawn, whereas virtually all T21-*XIST* hiPSCs

146 display *XIST* clouds and acquire H2A119ub/H3K27me3 signals in the presence of dox [Fig. 1B].
147 Together, these data illustrate the homogeneity of *XIST* induction, and provide additional
148 confirmation that this third copy of HSA21 is faithfully maintained in hiPSCs.

149 We next performed mRNA-seq of euploid, T21 and T21-XIST hiPSCs to confirm high
150 uniformity in pluripotency genes over lineage-specific markers [Fig. S2A], and to quantify T21
151 dosage correction by *XIST* in the presence, absence or upon withdrawal of dox [Fig. 1C,D], which
152 tests whether silencing is maintained once established. *XIST* is uniformly expressed in all three
153 T21-XIST clones at 3, 6 and 9 weeks (wks) of dox treatment ("+dox"), and returns to the ("-dox")
154 baseline upon dox withdrawal ["w/d", Fig. 1D], consistent with *XIST*-negative FISH in w/d samples
155 [Fig. 1B].

156 To accurately measure HSA21 dosage not only by standard differential expression analysis
157 but also HSA21 allelic representation, we additionally sequenced euploid and T21 whole
158 genomes (WGS) with linked-reads to identify and phase variants. In both euploid and T21 hiPSCs,
159 most variants can be grouped in large phase blocks (N50 lengths of 1.8 Mb and 2.9 Mb,
160 respectively), including across HSA21, where thousands of heterozygous variants distinguish the
161 *XIST*-bearing ($HSA21^{P}$) copy. Because all cell lines carry a single $HSA21^{P}$ copy, with one (D21) or
162 two (T21) $HSA21^{M/M2}$ copies, allele-specific phasing of mRNA-seq reads indeed reveals most
163 genes on HSA21 to express an average lesser allele frequency (LAF) of ~one-half for euploid (D21)
164 and ~one-third for T21 samples. Likewise, the *XIST*-bearing $HSA21^{P}$ copy (T21-XIST) is represented
165 in ~one-third of variant-mapping reads in the absence of dox (-dox), but is largely depleted in the
166 +dox and w/d samples, which were dox-treated (3wks) and collected after another 3 or 6 wks
167 without dox [Fig. 2A]. These data suggest that *XIST* silences most genes on the $HSA21^{P}$ copy near-
168 completely, and irreversibly, which is consistent with our expectations based on mouse *Xist*
169 reports (reviewed in [19]).

170 Likewise, differential expression analysis across all of HSA21 reveals the vast majority
171 genes with assessable expression are depleted by ~one-third (log2FC of -0.59, ±0.15), irrespective
172 of their linear distance from the *XIST* transgene, and maintain that expression level even after 3-
173 6 weeks of dox withdrawal [Fig. 2B-D]. Altogether, only a very small group of protein-coding
174 genes appears to retain a LAF > $1/6^{th}$ (*ADAMTS1, APP, H0Y3Z8, IFNAR1/2, MRPS6, ETS2* and *YBEY*),

175 although most are significantly downregulated by the expected degree ($p \leq 0.1$, log2FC -0.59, ±
176 0.15). Only *IFNAR2* and adjacent ORF *H0Y3Z8* also appear to escape *XIST*-mediated repression by
177 differential expression (p.adj > 0.1, log2FC > -0.3). To compare this efficacy to previously reported
178 T21-*XIST* systems [18,24,25], we considered the degree of silencing across all mutually assessed
179 HSA21 genes in prior reports, irrespective of adjusted p-value cutoff, as our study included a
180 greater number of samples. Indeed, we find that the distribution log2FC values in our T21-*XIST*
181 indicates more complete gene repression than what was observed in prior reports [Fig. S2B].
182 While we cannot rule out that this improved efficiency is due to some variation in the 13.9 kb
183 *XIST* cDNA transgene, TET3G promoters or applied dox concentration, we suspect that our
184 intergenic integration site may play an outsized role in magnitude and uniformity of transgene
185 induction.

186 Comparing differential expression in hiPSCs after 3 wk and 6wk of dox withdrawal, we
187 find that silencing is maintained in w/d samples, irrespective of the length of original dox
188 treatment [Fig. 2B, Fig. S2C]. We next assessed DNA methylation (DNAme, by Illumina methylEPIC
189 arrays) in T21-XIST samples, where essentially all CpGs at HSA21 promoters with low DNAme (all
190 ≤ 60% methylated with a median ≤ 8%) increase in DNAme to approximately the overall level
191 expected if 1 out of 3 alleles was fully methylated [Fig. 2F, all ≤ 60% methylated promoters with
192 medians of ~40% methylated for +dox]. This level is maintained after dox withdrawal (w/d), which
193 is consistent with the absence of reactivated genes by differential and allelic expression [Fig. 2A-
194 E].

195 We next turned to transcriptome-wide effects of T21 and *XIST*-corrected gene dosage.
196 While levels of HSA21 genes clearly increased in T21 relative to D21, and decreased in T21-XIST
197 +dox relative to -dox samples, all other chromosomes also responded to HSA21 dosage, albeit in
198 balanced fashion [Fig. 3A]. Consistently, samples with an effective HSA21 dosage matching
199 euploid samples (D21, and +dox or w/d T21-XIST) segregate from T21 and no-dox T21-XIST
200 samples in PCA [Fig. 3B]. Because our experimental design included the original, non-transgenic
201 D21 and T21 hiPSCs (198-1/2/5) with all treatments (±dox and w/d), we were able to observe
202 that their acute +dox treatment triggered expression changes that correlated with the T21
203 dosage effect [Fig. 3C top], which was still significant after exclusion of HSA21 genes from the

204 correlation [Fig. S3A, left]. This was not unexpected, because doxycycline can partially impact
205 mitochondrial translation in eukaryotic cells [45], and mitochondrial pathways are also altered in
206 DS [46–48]. We therefore adjusted for this small dox-specific effect in our analysis (see methods),
207 and compared these T21 over D21 log2FC expression changes with the combined (+dox and w/d)
208 *XIST* correction, revealing a highly significant and negative Pearson correlation of -0.5 [Fig. 3C,
209 bottom] that persists even when HSA21 genes are excluded [Fig. S3A, right]. These data indicate
210 that differentially expressed genes (DEGs) responding to excess HSA21 dosage are also changing
211 in the opposite direction when excess HSA21 dosage is corrected via *XIST*. This large-scale
212 reversal was also evident in gene-set enrichment analysis (GSEA), with a dominance of anti-
213 correlated terms [Fig. 3D, top left and bottom right quadrant], many of which related to
214 apoptosis, stress, ER, mitochondria and translation terms. Plotting the top three most-
215 concordant terms for each of these categories [Fig. 3E], T21 and dosage-corrected samples are
216 near uniformly opposed in biological processes previously implicated in DS, including apoptosis
217 [13,49,50], oxidative stress via NRF2 [12,51], mitochondria [14,46–48], and translation [10,52]. Importantly,
218 serine biosynthesis pathways, recently attributed to a general response to aneuploidy [16] were
219 also highly represented, indicating that serine metabolism returns to baseline upon T21 dosage
220 correction, despite the continued presence of the supernumerary HSA21 copy.

221 To assess T21 gene dosage effects in neural lineages, we applied a well-established
222 monolayer differentiation protocol that mimics *in vivo* neural development in the establishment
223 of neurogenic niches (rosettes) and in the production of both mature neurons and astrocytes
224 [53,54]. Use of this protocol was advantageous as most T21 hiPSC-derived neuronal RNA-seq to-date
225 was generated in immature neurons. We performed mRNA-seq in 10-12 wk neural cultures,
226 obtained 5-6 wks after low-density re-plating of 4 wk NPCs [Fig. S3B]. T21 neural cultures show
227 elevated HSA21 transcript levels with a peak at the expected +0.59 log2FC relative to euploid
228 samples [Fig. 4A,B]. As expected, neural and hiPSC DEGs and GSEA-enriched terms were
229 positively correlated, while neural GSEA terms were largely anti-correlated in direction with
230 terms enriched in XIST-corrected iPSCs [Fig. 4C-E], which also extended to the three most-
231 concordant terms across all comparisons [Fig. S3B]. Overall, we find *XIST*-mediated T21 dosage

232 correction to apply to a majority of significantly enriched terms differentiating T21 iPSCs and
233 neural cultures from their euploid controls [Fig. S4].

234 Staining for neuronal MAP2 and astroglial S100B markers, we noted an excess of
235 astrocytes in the T21 relative to euploid neural differentiations. Both neurons and astrocytes
236 derive from NPCs [55], and astrogliosis has been reported in DS models [31,33,34] and fetal samples
237 [26,28,30], where T21 NPCs prematurely shift from neurogenesis to astrogenesis. To determine
238 whether *XIST*-mediated T21-dosage correction could prevent this lineage skew, we first
239 confirmed that *XIST* expression and H2AK119ub enrichment would persist in 4 wk NPCs, which is
240 the case for well over 75% of NPCs derived across three independent clones, treated with +dox
241 as hiPSCs [Fig. 5A]. Indeed, even NPCs derived from untreated T21-*XIST* hiPSCs but receiving dox
242 from the first day of differentiation ("d0") have *XIST* and H2AK119ub foci in ≥75% and ≥65% of
243 all cells, respectively. Co-staining for MAP2 and S100B on day28 (4 wk) of neural differentiation
244 revealed a consistent and highly reproducible astrogenic skew in T21 and no-dox T21-XIST
245 samples relative to isogenic euploid control lines across multiple rounds of differentiation [Fig.
246 5B]. Remarkably, neurogenesis was fully rescued in neural differentiations from pre-treated as
247 well as d0+dox treated hiPSCs, across all three independent T21-XIST clones. Because the overall
248 sum of committed cells expressing either marker did not differ significantly between T21 and
249 euploid or T21-XIST dosage-corrected samples, we propose that T21 dosage does not suppress
250 NPC commitment in general, as suggested recently [24], but rather advances the shift to
251 astrogenesis, in line with prior reports [28,34].

252 Given the high rate of *XIST* induction in T21-XIST NPCs that only received dox at the onset
253 of differentiation (d0), we next explored whether the *XIST* transgene would remain dox-
254 responsive in terminally differentiated cells. To this end, we forced NPCs out of the cell cycle and
255 into terminal differentiation by inhibiting the Notch signaling pathway for 5 days (with gamma-
256 secretase inhibitor DAPT. Two days after completing this DAPT treatment, neural cultures were
257 treated with dox. To confirm DAPT treatment was sufficient to deplete mitotic cells, we also
258 labeled cells transiting S-phase with nucleotide analog EdU and co-stained for this label and *XIST*
259 FISH after 4 days of +dox exposure. DAPT-treated NPCs incorporating EdU comprise only ≤ 6% of
260 the neural population on average, whereas *XIST* is induced in ≥ 44% of cells [Fig. 6A]. Only ≤ 2%

261 are double-positive for Edu and *XIST* [Fig. 6A]. Edu incorporation therefore lacks any statistically
262 significant association with *XIST* induction, and may in fact be mildly anti-correlated, as only 26%
263 of Edu^{+} are also *XIST* $^{+}$ compared to ≥40% of Edu^{-} cells. We therefore conclude *XIST* is reliably
264 induced in sizeable fraction of post-mitotic T21-XIST cells that had not received dox prior to DAPT.
265 Finally, we assessed terminally differentiated cells that were treated with dox for 3 to 6
266 weeks after DAPT exposure ("pDAPT") to provide sufficient time for H2AK119ub enrichment. We
267 included "d0" controls that were treated with the standard 1 uM dox concentration throughout
268 neural diff, as well as low-dox "LD" samples, which were treated with 0.01 uM dox up to the DAPT
269 exposure, and standard 1 uM dox thereafter, to test whether "pre-marking" the TRE3G promoter
270 without effective induction may render it more responsive in terminal cell types. On average,
271 over half of d0 and LD cells featured prominent XIST clouds, followed by ≥ 40% of pDAPT samples,
272 across both c1 and c7 clones and in three independent rounds of differentiation. As before,
273 H2AK119ub signal lagged somewhat behind *XIST*, but consistently marked 27% - 36% of all cells
274 (58-65% compared to *XIST*), including MAP2-positive neurons and S100B-positive astrocytes [Fig.
275 6B]. We conclude, that our new T21-XIST transgene enables analysis of HSA21 dosage correction
276 in terminal and post-mitotic cell types, which will facilitate exploration of cellular and
277 transcriptional T21 hallmarks that may remain reversible after completed development.
278
279 **DISCUSSION**
280 The relevance of the inducible T21-XIST system presented herein extends from DS biology
281 and cellular responses to aneuploidy in general, to fundamental questions relating to human
282 *XIST*-mediated gene silencing and escape. In hiPSCs, our T21-XIST system is induced with near-
283 uniformity [Fig. 1], and corrects T21 dosage to euploid levels across HSA21 [Fig. 2], which we
284 demonstrate by inclusion of isogenic euploid control hiPSCs lines we derived in parallel from this
285 male donor with mosaic DS [36]. Leveraging phased sequence variants from linked-read WGS, we
286 can assign mRNA-seq reads allele-specifically to show that HSA21 genes derive half of their
287 expression from the $HSA21^{P}$ allele in euploid (D21) cells, and one-third in T21 cells, but nearly
288 extinguish expression from this *XIST*-bearing copy after dox induction [Fig. 2]. A small number of

289 genes retain some HSA21^{P} representation after dox, but are nonetheless significantly reduced in
290 differential expression to near-euploid levels.

291 This T21 dosage correction extends to genes responding to HSA21 dosage on other
292 chromosomes, reflecting a transcriptome-wide reversion of gene expression that moves dox-
293 exposed T21-XIST hiPSCs closer to their isogenic euploid controls [Fig. 3]. The balanced
294 experimental design and stability of T21 silencing after dox withdrawal (w/d) enable us to adjust
295 for dox effects that can inhibit mitochondrial translation [45] and selenocysteine incorporation [56].
296 GSEA reflects the large-scale reversion of T21-responsive cellular components, pathways and
297 functions [Fig. 3], including boosted expression of serine biosynthesis genes. These genes are
298 notable as dermal fibroblast of DS, as well as Patau (T13) and Edwards (T18) syndromes, all
299 depend on serine for proliferation [16]. Because these genes return to baseline upon correction of
300 T21 dosage [Fig. 3], despite maintenance of the HSA21 copy number, metabolic demand for
301 serine, while common to all three viable human autosomal aneuploidies, likely results from
302 expression of the supernumerary chromosome rather than its presence. We also find resurgent
303 expression of ribosomal protein genes and translation factors in T21-dosage corrected hiPSCs
304 [Fig. 3], which may be due to resetting the integrating stress response [10]. Indeed, cellular stress
305 pathways and apoptosis are dampened in response to T21 dosage correction, which is consistent
306 with the previously reported excess of apoptosis [13,49,50], mitochondrial dysfunction [14,46–48] and
307 oxidative stress [12,51] in DS.

308 In T21-driven expression of neural cultures, we find many of the same terms are enriched
309 by GSEA and concordant with T21 hiPSCs [Fig. 4]. In particular, T21-impacted mitochondrial
310 pathways and apoptotic terms [Fig. S3], as well as interferon response [Fig. S4], are exacerbated
311 in T21 neural cultures. Because these enriched terms and related genes responded to *XIST*-
312 mediated T21 dosage correction in hiPSCs, they likely reflect cellular phenotypes that depend on
313 ongoing excess HSA21 expression, and may therefore remain amenable to T21 dosage correction
314 after completed development.

315 In early neural differentiation, we observe that T21 NPCs produce an excess of astrocytes
316 at the expense of neurons [Fig. 5], which is consistent with astrogliosis noted in fetal DS [26,28,30].
317 Because *XIST*-mediated T21 silencing remains uniform into the NPC stage, neurogenesis is fully

318 rescued when T21-dosage is corrected prior to, and even during, neural differentiation [Fig. 5].
319 This is consistent with a prior report using T21-XIST dosage correction [24], but we can attribute
320 this neurogenic rescue to suppression of a conserved T21 astrogenic bias, rather than slowed
321 commitment of T21 NPCs [Fig. 6]. Several HSA21 genes have been suggested to play a role in this
322 astrogenic lineage bias, including amyloid precursor *APP, S100B*, and *DYRK1A* [28,34]. In addition, it
323 is possible that cellular stress pathways, such as oxidative stress that is elevated in DS hiPSC-
324 derived neurons and NPCs [40,57] and also implicates these and other HSA21 genes [12,28,51], impact
325 NPC lineage decisions, as seen in rodent models of neurogenesis [58].

326 We also examined T21-XIST hiPSC-derived mature neural lineages after forcing NPCs to
327 terminally differentiate and thus commit to either neuronal or astroglial cell fates via notch-
328 inhibitor DAPT. This more mature (~9-12wk), post-mitotic neural population [Fig. 6A], is
329 composed of a near equal number of terminally differentiated neurons and astrocytes [Fig. 5B].
330 Remarkably, a large fraction of these terminal post-mitotic cells remains able to express *XIST* and
331 deposit H2AK119ub on HSA21 in response to dox [Fig. 6B], regardless of whether they were never
332 exposed to dox prior to cessation of the DAPT treatment (post-DAPT, "pDAPT"), or were treated
333 with only a low (1% of the standard 1 uM) dox concentration prior to DAPT treatment. In contrast,
334 a previous T21-XIST system failed to be induced at all in post-mitotic monolayer neural cultures
335 [24], and another two reports could not assess *XIST* induction in terminal post-mitotic cells for
336 technical reasons [18,25].

337 Our results indicate our T21-*XIST* system represents a major improvement over these
338 prior systems [Fig. S2B], though several technical characteristics of transgene expression may
339 have contributed to this improvement. First, our system uses a *UBC-rTTA* construct integrated at
340 the AAVS "safe-harbor" locus, in contrast to prior studies that used EF1a [18] or CAG promoters [24]
341 at this locus, or re-delivered a high-copy *EF1α-rTTA* construct via piggyBac to NPCs [25]. Second,
342 there may be differences in the three individually-derived human *XIST* cDNA constructs on
343 account of sequence variation or splicing. And third, our *XIST* cDNA transgene was targeted
344 outside of *DYRK1A* to minimize its impact on *DYRK1A* prior to dox treatment, but also to avoid
345 attracting gene-body associated DNAme from overlapping transcription that serves to suppress
346 intragenic transcription start sites [59]. We suspect this last aspect to have contributed most, but

347 cannot rule out a confluence of AAVS1 regulation and/or rtTA promoter selection to play a role
348 as well.

349 Regarding *XIST* biology, our results suggest human neural lineages remain competent to
350 initiate *XIST*-mediated heterochromatin deposition even in the absence of DNA replication,
351 provided *XIST* can be induced. Apart from above mentioned reports on proliferative neural
352 progenitors [24,25], similar developmental plasticity in initiating [22,23], or re-initiating [17,60] *XIST*-
353 mediated repression was previously reported only for proliferative hematopoietic cell lineages.
354 Additionally, prior repots of *XIST* induction in human HT1080 fibrosarcoma cells indicate that
355 spreading of autosomal gene silencing remains reversible [61], and remains most effective near its
356 site of integration [62]. Both of these observations may be impacted in part by *XIST* repressing
357 haploinsufficient genes, which are not uncommon on mammalian autosomes, making whole or
358 partial trisomy a valuable research tool to better understands determinants of *XIST* spreading [63].
359 Indeed, our T21-XIST system repressed virtually every HSA21-linked gene without measurable
360 impact of its linear distance from the *XIST* integration site, across a large span of expression
361 values, and in irreversible fashion [Fig. 2]. Interestingly, the human inactive X in pluripotent stem
362 cells frequently undergoes progressive reactivation following loss of *XIST* expression [64], the order
363 of which we recently showed was determined in part by the distance to the nearest escapee gene
364 [65]. While our T21-XIST dox withdrawal was limited to 3-6 weeks, we found little evidence of
365 reactivation over this period, indicating that DNA methylation served to maintain T21 silencing
366 [Fig. 2]. Whether this remarkable epigenetic stability was due to the paucity of HSA21 genes
367 escaping XIST to seed potential reactivation, or the level of *XIST* prior to dox withdrawal, and to
368 which degree these two aspects are related, represent productive areas for future work.
369
370
371
372
373
374
375

376 **FIGURE LEGENDS**

377

378 **Figure 1: T21 hiPSCs induce *XIST* transgene and deposit heterochromatin on one HSA21 allele**

379 (A) Schematic of the TRE3G-XIST cDNA transgene integrated on $HSA21^P$

380 (B) Representative images (left) for XIST-FISH, and H2AK119ub and H3K27me3 IF, and image
381 quantification (right). A control panel of XIST negative 3wk w/d images for XIST-FISH are included.

382 (C) Schematic of cell lines and sample collection timepoints and dox treatment conditions.
383 Samples were collected after 3-9 wks of +dox or no-dox treatment, or 3 wk of +dox and 3 or 6
384 wks of dox withdrawal. A subset of samples was treated with dox for 2mo+ prior to
385 collection/withdrawal.

386 (D) *XIST* expression in T21-XIST samples from mRNA-seq (VST, variance-stabilized
387 transformed counts, approaching a log-transformation).

388

389 **Figure 2: *XIST*-mediated silencing extends across entire $HSA21^P$ and attracts DNAme**

390 (A) Representation of M/M2 and P alleles of all protein-coding HSA21 genes across dox
391 conditions and genotypes. Thick black line at 0.5 marks expected biallelic expression in euploid
392 (D21) cells, and dashed thin black line expected $1/3^{rd}$ representation for $HSA21^P$ allele in T21 cells.

393 (B) Heatmap showing VST counts normalized to the mean count in T21 samples (left panels)
394 for all expressed genes on HSA21.

395 (C) Distribution of log2(FC) (log2-foldChange) relative to no-dox T21 samples, for all
396 differentially expressed genes (DEGs, p.adj ≤ 0.1). "Combined" represents the differential
397 expression condition used in subsequent figures. Dashed black line represents the -0.59 log2FC
398 expected for complete T21 dosage correction. Blue and green shaded bands correspond to ±10%
399 and ±0.15 variation from a log2(FC) of -0.59.

400 (D) Log2(FC) values across HSA21 genes (arranged by position) compared to T21 samples.
401 Bubble colors shaded as indicated in the legend above, bubble size reflects base mean
402 expression.

403 (E) As in (B) but only displaying the genes with that maintain a LAF ≥ $1/6^{th}$ in allelic T21 mRNA-
404 seq in +dox or w/d conditions.

405 (F) Distribution of DNAme values from promoter-associated methylEPIC probes on HSA21
406 genes in T21-XIST no-dox, +dox, and w/d.
407
408 **Figure 3: Transcriptome-wide response to T21 gene dosage and correction via *XIST***
409 (A) Fraction of genes differentially expressed in response to T21 (top, relative to euploid) and
410 T21-XIST dosage correction (bottom, relative to T21 and no-dox) by direction (increasing,
411 decreasing, or unchanged, ~0) and by chromosome.
412 (B) PCA of all mRNA-seq samples, batch-corrected for timepoint and dox status. Open
413 symbols for original euploid (198-1/2) and T21 (198-5) lines, closed symbols for T21-XIST
414 transgenic lines (c1/4/7). Colors indicate effective HSA21 dosage as indicated in Figures 1 and 2
415 (w/d colored separately to distinguish from +dox T21-XIST samples).
416 (C) Overlap of differential expression between hiPSC T21/D21 (y-axis) over the dox effect
417 (top, non-transgene +dox/no-dox) or T21-XIST dosage correction (T21XIST+dox & withdrawal /
418 T21). Adjusted p-values were combined (C.padj, calculated using Fisher's method) for all DEGs,
419 and colored by -log10(C.padj) provided C.padj ≤0.1 (or grey for C.padj > 0.1). Linear regression is
420 plotted along with the Spearman correlation coefficient and p-value for all genes.
421 (D) Overlap of enriched GSEA terms comparing normalized enrichment scores (NES) for hiPSC
422 T21/D21 over dosage-corrected T21-XIST/T21. Bubble plots corresponds to the -log10(combined
423 pvalue by Fisher's method). Colors denote chosen categories (all with combined pvalue ≤ 0.2).
424 (E) Individual significantly-enriched terms (combined p ≤ 0.1) from each of the categories in
425 (D), selected by a concordance measure (euclidean distance from origin in D). Colors denote NES,
426 bubble size the individual -log10(p.adj).
427
428 **Figure 4: Concordant T21 dosage imbalance and transcriptomic response after neural**
429 **differentiation**
430 (A) Heatmap showing VST counts normalized to the mean count in T21 neural samples (left
431 panels) for all expressed genes on HSA21.
432 (B) Distribution of log2(fold-change) from HSA21 genes comparing neural T21 to D21. Dashed
433 black line denotes expected log2(FC) of +0.59 (all HSA21 genes shown, irrespective of p.adj).

434 (C) Overlap of differential expression between hiPSC T21/D21 (y-axis) over neural T21/D21
435 samples (x-axis). Adjusted p-values were combined and colored as in Fig. 3C, with linear
436 regression plotted (Spearman coefficient and p-value for all genes).
437 (D) Overlap of enriched GSEA terms comparing normalized enrichment scores (NES) for hiPSC
438 T21/D21 (y-axis) over neural T21/D21. Bubble plots corresponds to the -log10(combined pvalue
439 by Fisher's method). Colors denote chosen categories (all with combined pvalue ≤ 0.2).
440 (E) As in (D) but combining neural T21/D21 GSEA (x-axis) with GSEA of dosage-corrected T21-
441 XIST hiPSCs (hiPSC rescue) on the y-axis.
442
443 **Figure 5: Early astrogenesis at neurogenic expense is suppressed by T21 dosage correction prior**
444 **to NPC stage**
445 (A) Representative images (left) and quantification (right) of H2AK119ub (IF) and XIST (FISH)
446 signal after neural differentiation from dox treated cells. Dox treatment was either started while
447 cells were hiPSCs (top), or on the first day of differentiation ("d0", bottom).
448 (B) Relative lineage commitment to astrocytes (s100b) or neurons (MAP2) in euploid, T21,
449 and T21-XIST cells under different dox treatments. Error bars represent the standard error of the
450 mean based on the number of rounds of differentiation.
451 (C) Representative images at D28 of neural differentiation in euploid (left column), trisomic
452 (center column) and rescued (right column) labeled for neuronal MAP2 (red), astroglial S100B
453 (green) and H2AK119ub accumulating on HSA21 (white). Insets display H2AK119ub foci are sen
454 in astrocytes and neurons alike.
455
456 **Figure 6: T21-XIST transgene remains inducible and attracts H2AK119ub in post-mitotic**
457 **neurons and astrocytes**
458 (A) *XIST* (red) and EdU (green) quantification on D36 of neural differentiation (4 days
459 following completion of DAPT treatment and beginning dox treatment). Less than 6% of
460 cells were EdU+ (green), EdU+XIST+ cells represented less than 2% of total cells.
461 (B) Representative images (left) and quantification (right) of H2AK119ub (yellow) IF and XIST-
462 FISH (red) signal after neural differentiation from different dox treatments.

463 **SUPPLEMENTARY FIGURE LEGENDS**

464

465 **Figure S1**

466 (A) Taqman copy number (CN) assay for 21q22 (*DYRK1A*) in GM00260-derived hiPSC clones.

467 (B) Taqman CN assay for 17q25 (*SEC14L1*) in GM00260-derived hiPSC clones.

468 (C) DNA SureFISH for chr21q, and FastFISH chrX, chr8, chr12, and chr17 centromeres in 198-

469 6/8 with counts and images denoting the dominant staining pattern.

470 (D) Summary of CytoSNP850k calls across GM00260 and its reprogrammed hiPSC clones. Calls

471 marked with a red 'x' were common across all lines, including donor fibroblasts. Call marked with

472 a small 'x' were line-specific, except for T21 (denoted by a capital 'X').

473 (E) Absolute difference in allele (theta) frequency of CytoSNP850k probes comparing T21 and

474 euploid clones (D21), colored by T21-specific base calls (red/blue) and hetero/homozygosity

475 (grey and yellow, respectively).

476 (F) DNA FISH against DSCR8 (Vysis, LSI21) in interphase and metaphase spreads of validated

477 hiPSC clones, with counts and images denoting the dominant staining pattern.

478 (G) Taqman CN assay for 21q22 (*DYRK1A*) across all AAVS-rTTA subclones of T21 198-5 hiPSCs.

479

480 **Figure S2**

481 (A) Germ layer-specific and pluripotency marker expression across the euploid (198-1/2),

482 T21 (198-5), and transgenic T21-XIST (c1/4/7) hiPSC lines.

483 (B) Change in log2-transformed expression relative to corresponding T21 samples in this and

484 the two referenced T21-XIST studies. Mean difference of HSA21 gene expression comparing w/d

485 T21-XIST samples and T21 samples. Line type denotes the length of the initial dox treatment, and

486 color the duration of dox w/d.

487 (C) Mean difference of HSA21 gene expression comparing w/d T21-XIST samples and T21

488 samples. Line type denotes the length of the initial dox treatment, and color the duration of dox

489 w/d.

490

491

492 **Figure S3**

493 (A) Same as Fig. 3C but excluding HSA21 genes: overlap of differential expression between
494 hiPSC T21/D21 (y-axis) over the dox effect (top, non-transgene +dox/no-dox) or T21-XIST dosage
495 correction (T21XIST+dox & withdrawal / T21). Adjusted p-values were combined (C.padj,
496 calculated using Fisher's method), and colored by -log10(C.padj) provided C.padj ≤0.1 (or grey for
497 C.padj > 0.1). Linear regression is plotted along with the Spearman correlation coefficient and p-
498 value for all non-HSA21 genes.

499 (B) Individual significantly-enriched terms (combined p ≤ 0.1) from each of the categories in
500 Fig. 4(D,E), selected by a concordance measure (euclidean distance from origin in D). Colors
501 denote NES, bubble size the individual -log10(p.adj).

502

503 **Figure S4**

504 Comparison of terms over-represented in GSEA across hiPSC T21, neural T21, T21 dosage
505 correction ("rescue"), and the dox-effect in non-transgenic hiPSCs. Terms from Hallmark, KEGG,
506 and WikiPathways (WP) are shown. All terms are sorted by hiPSC T21 NES (normalized
507 enrichment score from GSEA), with a p.adj thresholds of p ≤ 0.1 for hiPSC T21, and additionally
508 p.adj ≤ 0.2 for the three additional panels (neural T21, T21 rescue, and dox-effect).

509

510

511

512

513

514

515

516

517

518

519

520

521 **MATERIALS & METHODS**

522

523 **Reprogramming, hiPSC validation and culture**

524 Human male fibroblast line (GM00260) mosaic for trisomy 21 (T21) was obtained from the Coriell
525 Institute (Camden, NJ) and reprogrammed by the University of Connecticut's Cell and Genome
526 Engineering Core, using the CytoTune hiPSC 2.0 Sendai Reprogramming kit (Thermo Fisher
527 Scientific, Waltham, MA). Genomic DNA from hiPSC clones was screened via duplex Taqman Copy
528 Number (CN) Assay (*DYRK1A* - Hs01748441_cn and RNaseP, Thermo Fisher Scientific) to select
529 euploid and T21 lines, followed by additional screening for Chr17q Taqman CN assay (*SEC14L1*,
530 Hs05476397_cn), and the hPSC Genetic Analysis Kit (Stemcell Technologies, Vancouver, Canada).
531 Interphase and M phase nuclei were also screened via FASTFISH (WiCell, Madison, WI) using Chr
532 20q (BCL2L1) and centromere enumeration probes for Chr 8, 12, 17, and X, alongside a SureFISH
533 assay for Chr 21q (DSCR8). Selected hiPSC lines were further screened by aCGH (Infinium
534 BeadChip CytoSNP 850K assay, Illumina, San Diego, CA) at the Center for Genome Innovation,
535 Institute for Systems Genomics at the University of Connecticut.
536 T21 and euploid hiPSCs were cultured on mitotically inactive mouse embryonic fibroblasts (mEFs)
537 in standard hiPSC media in 5% CO_2 at 37°C (80% DMEM/F12, 20% Knockout Serum Replacement,
538 1% Glutamax, 1% Non-Essential Amino Acids, 0.1% ß-Mercaptoethanol, and 8ng/mL bFGF,
539 Thermo Fisher Scientific), and passaged weekly by manual disruption of 6-10 representative
540 colonies. For hiPSC cultures requiring doxycycline induction, 2µM doxycycline was added to the
541 culture media.

542

543 **Neural differentiation**

544 T21 and euploid hiPSCs were passaged manually onto mEFs and in hiPSC medium. On day 2 post-
545 passage, cultures were switched into N2B27 neural differentiation medium (Neurobasal medium
546 (Gibco), 2% B27 (Gibco), 1% N2(DMEM:F12 (Gibco), 25ug/ml insulin (Sigma), 100ug/ml holo-
547 transferrin, 100uM putrescine, 20nM progesterone, 30nM selenite), 1% ITS-A (Gibco), 1%
548 Penicillin-Streptomycin (Gibco), and 1% Glutamax (Gibco), supplemented with noggin at 500
549 ng/ml (R&D Systems). Cultures were fed and supplemented with Noggin every other day through

550 day 10. For neural differentiation with doxycycline induction, 1 µM doxycycline ,or 0.01 µM for
551 low-dose cultures, was added to the culture media. Cultures were fed N2B27 until the
552 appearance of mature rosette structures (D14-D16). Rosette-stage cultures were passaged
553 manually 1:1 onto poly-d-lysine (PDL) and laminin-coated tissue culture plates and grown to
554 confluence. Cells were cultured until D23 and passaged enyzmatically with Accutase (Invitrogen)
555 onto PDL and laminin-coated substrates at 1.9x10^4/cm2- 2.2x10^4. At D25, cultures were
556 switched to Neural Differentiation medium (NDM) (Neurobasal medium (Gibco), 2% B27 (Gibco),
557 1% non-essential amino acids (NEAA; Gibco), 1% Penicillin-Streptomycin (Gibco) 2mM Glutamax
558 (Gibco) 10 ng/ml brain-derived neurotrophic factor (BDNF; Peprotech), 10ng/ml glial-derived
559 neurotrophic factor (GDNF; Peprotech), 1uM cyclic AMP (cAMP;Sigma), and 200uM ascorbic acid
560 (AA; Sigma). Cells were cultured in NDM until assay endpoint. For DAPT-treated cultures, DAPT
561 (Tocris Bioscience) was added for 5 days at 10uM.
562
563 **Nucleic acid purification**
564 Genomic DNA was purified from fresh or frozen pelleted cells using three different methods
565 depending on application. For colony PCR screening, genomic DNA was extracted via standard
566 high-salt chloroform extraction. For standard PCR, and array hybridization, cell pellets were
567 resuspended in either cell lysis buffer 1 (10 mM Tris-HCl, pH 8.0; 100 mM NaCl; 10 mM EDTA, pH
568 8.0; 1% SDS; 200 µg/ml Proteinase K), or cell lysis buffer 2 (10 mM Tris-HCl, pH 8.0; 200 mM NaCl;
569 10 mM EDTA, pH 8.0, 0.5% Sarcosyl; 1 mg/mL Proteinase K) and incubated at 55°C for 3 hours to
570 overnight with optional RNAse A, 10 ug/mL treatment following at 37C for 5 minutes. Genomic
571 DNA was isolated using Phenol:Chloroform:Isoamyl Alcohol (25:24:1, v/v) (Invitrogen, Waltham,
572 MA), precipitated with either isopropanol or 300 mM sodium acetate with 2 volumes of 100%
573 chilled ethanol and 15 minutes at -80C, washed with 70% ethanol, and resuspended in TE buffer.
574 For linked-read WGS, high molecular weight (HMW) genomic DNA was prepared from fresh or
575 frozen iPS cell pellets, following the protocol listed in the Chromium Genome Reagent Kits v2
576 User Guide (10x Genomics, Pleasanton, CA), using the MagAttract HMW Kit (Qiagen,
577 Germantown, MD) with minor modifications.

578 Plasmid and fosmid DNA was purified with either the Zyppy Plasmid Miniprep kit or ZymoPURE II
579 Plasmid Midiprep kit (Zymo Research, Irvine, CA). Following restriction digests or PCR, DNA
580 purification was performed with the Monarch PCR & DNA Cleanup kit (New England Biolabs,
581 Ipswich, MA), or the DNA Clean & Concentrator Kit (Zymo Research). For RNA isolation, the
582 PureLink RNA Mini Kit (Invitrogen, Carlsbad, CA) was used, followed by cDNA synthesis using the
583 iScript gDNA Clear cDNA Synthesis Kit (Bio-Rad Laboratories, Hercules, CA).
584
585 **Quantitative RT-PCR**
586 Gene expression was measured via qRT-PCR using the iTaq Universal SYBR Green Supermix (Bio-
587 Rad Laboratories) and the ΔCt method. Primer specificity was confirmed by melting curve
588 analysis, and relative expression was calculated as %GAPDH ($100/2^{\Delta Ct}$). Taqman CN assays were
589 normalized to 198-1 genomic DNA. HOT FIREPol Probe Universal PCR Mix Plus - no ROX (Solis
590 BioDyne, Tartu, Estonia) was used per manufacturer's instructions, using 4 ng of high-quality
591 genomic DNA template in 20 ul reactions. The hPSC Genetic Analysis Kit (Stemcell Technologies)
592 was used following the manufacturer's instructions. All qPCR reactions were performed in
593 triplicate in a Bio-Rad CFX 96 Real-Time System.
594
595 **Plasmid construction**
596 For PCR amplifications, either Herculase II polymerase (Agilent, Santa Clara, CA), Platinum Taq
597 High Fidelity (Thermo Fisher Scientific), Advantage 2 polymerase (TaKaRa Bio, Shiga, Japan), or
598 Q5 Hi-Fidelity DNA Polymerase (New England Biolabs) was used. For cloning reactions except the
599 large *XIST* insert steps, ligations were performed with T4 DNA ligase, 2,000,000 units/mL (New
600 England Biolabs) and DH10B homemade chemically competent cells were used at 37°C. For all
601 cloning with XIST cDNA fragments aside from ligation of oligo not followed by transformation
602 (which used the same T4 DNA ligase), the TaKaRa DNA Ligation Kit LONG (TaKaRa Bio) was used
603 along with NEB Stable Competent E. coli (New England Biolabs) with bacterial incubations at 25-
604 30°C to mitigate instability in initial steps observed at 37°C.
605 To clone the XIST transgene cDNA in a temporary pUC19 vector, a 10 kb fragment containing
606 most of XIST exon 1 was cut from a fosmid (WI2-935P22, BACPAC Genomics) with SacII and PshAI.

607 Linker oligos were used to clone the 10 kb SacII and PshAI fragment into the KpnI and XbaI sites
608 of pUC19, respectively. The 5'-most end of *XIST* exon 1 was PCR amplified, concurrently adding a
609 5' PmeI restriction site. The resulting PCR product was digested with PmeI and BtgZI and cloned
610 in between the PmeI/BtgZI restriction sites of the XIST exon 1-containg plasmid. The 3' end of
611 exon 1 through through exon 6 was amplified from cDNA of Wi-38 cells (AG07217, Coriell
612 Institute), while adding a 3' SalI restriction site. The resulting PCR was digested with PshAI and
613 SalI and cloned between the PshAI and SalI sites of the plasmid from the prior step to complete
614 the XIST cDNA construct.
615 The *UBC* promoter from the FUGW construct [66] (Addgene plasmid #14883) was cloned into
616 AAVS1-Neo-M2rtTA [67] (Addgene plasmid #60843). The *UBC* promoter was PCR-amplified with
617 flanking PvuII and FseI sites, and cloned into the AleI and FseI sites on the AAVS1-neo-M2rtTA
618 plasmid. This rtTA-advanced ORF was replaced with rtTA3G from the pCMV-Tet-3G plasmid (
619 TaKaRa Bio), by by XbaI and XmaI digestion and cloning of three separate fragments to create
620 the final rtTA vector AAVS1-NEO-UBrtTA-3G.
621 To generate the final targeting vector, pTRE3G (TaKaRa Bio) was used as the backbone, following
622 excision of an XbaI fragment to reduce the size of the vector via removal of the SV40 small intron,
623 NLS, and SV40 polyA sequences. The 5' homology arm for Ch21 was generated by PCR with EcoRI
624 sites on each primer using the genomic DNA of the destination cell line as the template. This PCR
625 product was ligated into the EcoRI sites of the pTRE3G vector to make pTRE3G-5P. Next a fusion
626 PCR product was generated, harboring a BGH polyA amplified from pl452 [68] and the 3' homology
627 arm using overlapping PCR from the genomic DNA of the destination cell line. This PCR product
628 was cloned into the PstI and BamHI sites of the pTRE3G-5P to make pTRE3G-5P3P. Next a loxp-
629 flanked PGK-puro-TK fragment was removed from vector pl452-puroTK by XhoI digest. The
630 fragment was cloned into the XhoI sites of the vector pTRE3G-5P3P. This pl452-puroTK vector
631 was derived from plasmids pl452 and plasmid pLCA.66/2272 [69] (Addgene plasmid #22733) by
632 removing the PGKpuroTK with AgeI and BbsI and cloning that fragment into pl452 using the same
633 enzymes. To add the XIST cDNA construct, this CMV-puroTK-TRE3G vector was digested with
634 MluI and SbfI, and a phosphorylated linker oligo was ligated to purified, digested backbone,
635 creating a SacI-compatible overhang. Following purification, this vector was ligated to the SbfI-

636 SacI fragment containing the *XIST* cDNA construct, to create the TRE3G-XIST cDNA targeting
637 vector.
638
639 **hiPSC targeting and screening**
640 Targeting was performed using a Lonza Nucleofector 4D (Lonza, Basel, Switzerland) with primary
641 cell kit P3 and program CD-150. AAVS1-Neo-ubrtTA was targeted to HSA21 of the T21 cell
642 line 198-5. Two ug of each AAVS1-targeting TALEN [70] was nucleofected along with 6 ug of AAVS1
643 integration vector. Cells were plated on mitotically inactivated DR4 MEFs (ATCC, Manassas,
644 Virginia) post-nucleofection. After 96 hours, cells were cultured with G418 at a concentration of
645 25 ug/ml. Selection was done for a total of 6 days. Resulting colonies were isolated and screened
646 for targeting. cDNAs from targeted clones were tested for expression of rtTA by RT-qPCR. AAVS1
647 TALEN-L (Addgene plasmid #59025) and AAVS1 TALEN-R (Addgene plasmid #59026) were used
648 for targeting the UBrtTA. Integrants were screened using (AAVS1 scr F/Neo R and AAVS1 3'scr
649 R/rtTA F). For targeting XIST transgene via CRISPR, guides designed to target the HSA21P copy
650 without cutting the HSA21$^{M/M2}$ alleles were cloned into PX459V2 (Addgene plasmid #48139) at
651 the BbsI site by annealing and ligating overlapping oligos. Two ug each this CRISPR guide plasmid
652 was used along with 6 ug XIST cDNA targeting vector. Cells were plated on DR4 MEFs and after
653 96 hours, puromycin was added to the culture at a concentration of 0.5 ug/ml for a total of 4
654 days. Resulting colonies were isolated and genotyped for targeting by PCR. Clones were verified
655 by sequencing across the target to verify the loss of the targeted allele.
656
657 **Immunofluorescence and *XIST* RNA-FISH**
658 For *XIST* RNA FISH,cells were permeabilized with 0.5% Triton-X and 2mM ribonucleoside vanadyl
659 complex (RVC) in CSK Buffer (10mM PIPES pH 6.8, 100mM NaCL, 3mM MgCl2, 300nM sucrose),
660 fixed in 4% PFA in PBS, then dehydrated through a series of ethanol washes (70%,80%, 90%, and
661 100%). Digoxigenin-labeled XIST probe hybridization was performed overnight in a humidity
662 chamber at 42°C. Anti-digoxigenin antibody (ThermoFisher; 700772) was hybridized for 1 hour at
663 RT. Secondary antibody hybridization (Alexa Fluor; Invitrogen; 1:500) followed for 1 hour at RT.

664 Nuclear DNA was counter-stained with Hoechst 33342 dye. Slides were imaged with an EVOS FL
665 Auto2 system (Thermo Fisher Scientific). [71]
666 For immunofluorescence cells were grown in Nunc Lab-Tek II glass chamberslides coated with
667 poly-d-lysine and laminin (for neural differentiation) or permanox chamberslides with MEFs
668 (iPSCs). Cells were fixed in 4% paraformaldehyde (Electron Microscopy Sciences, Hatfield, PA) for
669 10 minutes at room temperature (RT), rinsed with PBS 3 times for 5 minutes and then
670 permeabilized in 1% Triton-X in PBS for another 10 minutes. Samples were blocked in blocking
671 buffer containing PBS, 0.1% Triton-X, 5% BSA and 2% normal goat serum (MilliporeSigma). Cells
672 were placed in antibodies diluted in blocking buffer overnight at 4°C in a humidity chamber.
673 Primary antibodies were used as follows: MAP2 (Abcam; ab5392; 1:10,000), S100B (Sigma; s2532;
674 1:1000), H2AK119ub (Cell Signaling; 8240, 1:1600). Following washes in 0.1% Triton-X in PBS, 3
675 times for 5 minutes, cells were labeled with Alexa Fluor secondary antibodies at 1:500 for 1 hour
676 at RT. Nuclei were counterstained withHoechst 33342and slides preserved in Prolong Gold
677 Antifade Mountant (Thermo Fisher Scientific). IF and FISH automated image quantification was
678 performed using a custom CellProfiler pipeline [71].
679
680 **Cytogenomics, DNA methylation, Linked-read WGS and mRNA sequencing**
681 For cytogenomic analysis, genomic DNA was labeled and hybridized to the Infinium BeadChip
682 CytoSNP 850K array (Illumina, San Diego, CA) according to the manufacturer's protocols. For
683 DNAme analysis, genomic DNA was bisulfite-converted using the EZ DNA Methylation Kit (Zymo
684 Research, Irvine, CA), then labeled and hybridized using the Infinium Methylation EPIC BeadChip
685 Kit (Illumina) following standard protocol of each manufacturer. Both types of arrays were
686 scanned on a NextSeq 550 system (Illumina).
687 HMW genomic DNA was sequenced to ~30x coverage on a NovaSeq 6000 (Illumina), following
688 library preparation on the 10X Genomics Linked-Read platform at the Center for Genome
689 Innovation, Institute for Systems Genomics at the University of Connecticut. For standard mRNA-
690 seq, libraries were prepared using the Illumina stranded mRNA Kit and 100bp paired-ends reads
691 were sequenced to an average depth pf 40 million reads/replicate on the NovaSeq 6000 (Illumina,
692 San Diego, CA).

693

694 **Expression and DNA methylation analysis**

695 The FASTQ files were quality controlled using FASTQC, reads were filtered and adapter-trimmed
696 was done using BBDuk [72]. Expression quantification was performed using Salmon [73], and
697 differential expression analysis was performed using DESeq2 [74]. Gene set enrichments were
698 performed using the GSEA function from the R package clusterProfiler [75] on the following gene
699 sets: Biocarta, GO (Biological Processes, Cellular Components, and Molecular Functions), KEGG,
700 Pathway Interaction Database, Reactome, and WikiPathways. For DNAme analysis, the
701 MethylEPIC IDAT files were processed using the R package minfi and its preprocessIllumina
702 function to obtain methylation β-values [76]. Promoter probes were defined as having one of the
703 following designations in the array manifest file: TSS1500, TSS200, or 5_UTR.

704

705 **Phased allelic RNA-seq analysis**

706 The 10X Genomics Long Ranger pipeline was used to align reads, and call and phase SNPs, indels,
707 and structural variants from linked-read WGS reads. The processed FASTQs from above were
708 aligned using HISAT2 to the hg38 human reference genome [77]. Relevant HSA21 SNPs were
709 extracted from the Long Ranger output and used to get haplotype gene expression counts from
710 aligned RNA-seq bam files using the phASER software package [78]. While this provided reliable
711 intragenic phasing, for intergenic phasing on chr21 we relied on the imbalanced haplotype gene
712 expression in the T21, compared to its isogenic euploid controls. The higher expressed haplotype
713 was designated as the major (duplicated or $HSA21^{M/M2}$) haplotype and the other as the minor
714 haplotype ($HSA21^{P}$).

715

716

717

718

719

720

721

ACKNOWLEDGEMENTS

We thank the University of Connecticut's Cell and Genome Engineering Core and Center for Genome Innovation for reprogramming, as well as mRNA-seq, CytoSNP, linked-read WGS and methylEPIC core services, respectively. This work was supported by grants from the LuMind IDSC Foundation and the NIH (R35GM124926) to S.F.P.

DECLARATION OF INTERESTS

No competing interests

REFERENCES

1. Capone, G. T., Chicoine, B., Bulova, P., Stephens, M., Hart, S., Crissman, B., *et al.* Co-occurring medical conditions in adults with Down syndrome: A systematic review toward the development of health care guidelines. *Am. J. Med. Genet. Part A* **176**, 116–133 (2018).
2. Antonarakis, S. E., Skotko, B. G., Rafii, M. S., Strydom, A., Pape, S. E., Bianchi, D. W., *et al.* Down syndrome. *Nat. Rev. Dis. Prim.* **6**, 1–20 (2020).
3. Kazuki, Y., Gao, F. J., Li, Y., Moyer, A. J., Devenney, B., Hiramatsu, K., *et al.* A non-mosaic transchromosomic mouse model of down syndrome carrying the long arm of human chromosome 21. *Elife* **9**, 1–29 (2020).
4. Herault, Y., Delabar, J. M., Fisher, E. M. C., Tybulewicz, V. L. J., Yu, E. & Brault, V. Rodent models in Down syndrome research: impact and future opportunities. *Dis. Model. Mech.* **10**, 1165–1186 (2017).
5. Bhattacharyya, A. Advancing knowledge of down syndrome brain development and function with human stem cells. *Am. J. Intellect. Dev. Disabil.* **25**, 90–92 (2020).
6. Suzuki, I. K. & Vanderhaeghen, P. Is this a brain which i see before me? Modeling human neural development with pluripotent stem cells. *Development (Cambridge)* vol. 142 3138–3150 (2015).
7. van den Ameele, J., Tiberi, L., Vanderhaeghen, P. & Espuny-Camacho, I. Thinking out of the dish: what to learn about cortical development using pluripotent stem cells. *Trends Neurosci.* **37**, 334–42 (2014).
8. Wiseman, F. K., Al-Janabi, T., Hardy, J., Karmiloff-Smith, A., Nizetic, D., Tybulewicz, V. L. J., *et al.* A genetic cause of Alzheimer disease: Mechanistic insights from Down syndrome. *Nature Reviews Neuroscience* vol. 16 564–574 (2015).
9. Rosi, S. & Frias, E. S. The Integrated Stress Response: A Central Memory Switch in Down Syndrome. *Cell Metab.* **31**, 15–17 (2020).
10. Zhu, P. J., Khatiwada, S., Cui, Y., Reineke, L. C., Dooling, S. W., Kim, J. J., *et al.* Activation of the ISR mediates the behavioral and neurophysiological abnormalities in down syndrome. *Science (80-.).* **366**, 843–849 (2019).

761 11. Tramutola, A., Lanzillotta, C., Arena, A., Barone, E., Perluigi, M. & Di Domenico, F.
762 Increased Mammalian Target of Rapamycin Signaling Contributes to the Accumulation of
763 Protein Oxidative Damage in a Mouse Model of Down's Syndrome. *Neurodegener. Dis.*
764 **16**, 62–68 (2016).
765 12. Zamponi, E., Zamponi, N., Coskun, P., Quassollo, G., Lorenzo, A., Cannas, S. A., *et al.* Nrf2
766 stabilization prevents critical oxidative damage in Down syndrome cells. *Aging Cell* **17**,
767 e12812 (2018).
768 13. Helguera, P., Pelsman, A., Pigino, G., Wolvetang, E., Head, E. & Busciglio, J. ets-2
769 promotes the activation of a mitochondrial death pathway in Down's syndrome neurons.
770 *J. Neurosci.* **25**, 2295–303 (2005).
771 14. Helguera, P., Seiglie, J., Rodriguez, J., Hanna, M., Helguera, G. & Busciglio, J. Adaptive
772 downregulation of mitochondrial function in down syndrome. *Cell Metab.* **17**, 132–40
773 (2013).
774 15. Di Domenico, F., Coccia, R., Cocciolo, A., Murphy, M. P., Cenini, G., Head, E., *et al.*
775 Impairment of proteostasis network in Down syndrome prior to the development of
776 Alzheimer's disease neuropathology: Redox proteomics analysis of human brain.
777 *Biochim. Biophys. Acta - Mol. Basis Dis.* **1832**, 1249–1259 (2013).
778 16. Hwang, S., Cavaliere, P., Li, R., Zhu, L. J., Dephoure, N. & Torres, E. M. Consequences of
779 aneuploidy in human fibroblasts with trisomy 21. *Proc. Natl. Acad. Sci.* **118**, e2014723118
780 (2021).
781 17. Chiang, J. C., Jiang, J., Newburger, P. E. & Lawrence, J. B. Trisomy silencing by XIST
782 normalizes Down syndrome cell pathogenesis demonstrated for hematopoietic defects in
783 vitro. *Nat. Commun.* **9**, (2018).
784 18. Jiang, J., Jing, Y., Cost, G. J., Chiang, J.-C., Kolpa, H. J., Cotton, A. M., *et al.* Translating
785 dosage compensation to trisomy 21. *Nature* **500**, 296–300 (2013).
786 19. Pinter, S. F. A Tale of Two Cities: How Xist and its partners localize to and silence the
787 bicompartmental X. *Semin. Cell Dev. Biol.* **56**, 19–34 (2016).
788 20. Wutz, A. & Jaenisch, R. A shift from reversible to irreversible X inactivation is triggered
789 during ES cell differentiation. *Mol. Cell* **5**, 695–705 (2000).
790 21. Kohlmaier, A., Savarese, F., Lachner, M., Martens, J., Jenuwein, T. & Wutz, A. A
791 chromosomal memory triggered by Xist regulates histone methylation in X inactivation.
792 *PLoS Biol* **2**, E171 (2004).
793 22. Savarese, F., Flahndorfer, K., Jaenisch, R., Busslinger, M. & Wutz, A. Hematopoietic
794 precursor cells transiently reestablish permissiveness for X inactivation. *Mol. Cell. Biol.*
795 **26**, 7167–77 (2006).
796 23. Agrelo, R., Souabni, A., Novatchkova, M., Haslinger, C., Leeb, M., Komnenovic, V., *et al.*
797 SATB1 defines the developmental context for gene silencing by Xist in lymphoma and
798 embryonic cells. *Dev. Cell* **16**, 507–516 (2009).
799 24. Czermiński, J. T. & Lawrence, J. B. Silencing Trisomy 21 with XIST in Neural Stem Cells
800 Promotes Neuronal Differentiation. *Dev. Cell* (2020) doi:10.1016/j.devcel.2019.12.015.
801 25. Kawatani, K., Nambara, T., Nawa, N., Yoshimatsu, H., Kusakabe, H., Hirata, K., *et al.* A
802 human isogenic iPSC-derived cell line panel identifies major regulators of aberrant
803 astrocyte proliferation in Down syndrome. *Commun. Biol.* **4**, 730 (2021).
804 26. Guidi, S., Bonasoni, P., Ceccarelli, C., Santini, D., Gualtieri, F., Ciani, E., *et al.* Neurogenesis

805 impairment and increased cell death reduce total neuron number in the hippocampal
806 region of fetuses with Down syndrome. *Brain Pathol.* **18**, 180–197 (2008).
807 27. Zdaniuk, G., Wierzba-Bobrowicz, T., Szpak, G. M. & Stępień, T. Astroglia disturbances
808 during development of the central nervous system in fetuses with Down's syndrome.
809 *Folia Neuropathol.* **49**, 109–114 (2011).
810 28. Lu, J., Esposito, G., Scuderi, C., Steardo, L., Delli-Bovi, L. C., Hecht, J. L., *et al.* S100B and
811 APP promote a gliocentric shift and impaired neurogenesis in down syndrome neural
812 progenitors. *PLoS One* **6**, (2011).
813 29. Lu, J., Lian, G., Zhou, H., Esposito, G., Steardo, L., Delli-Bovi, L. C., *et al.* OLIG2 over-
814 expression impairs proliferation of human Down syndrome neural progenitors. *Hum.*
815 *Mol. Genet.* **21**, 2330–2340 (2012).
816 30. Guidi, S., Giacomini, A., Stagni, F., Emili, M., Uguagliati, B., Bonasoni, M. P., *et al.*
817 Abnormal development of the inferior temporal region in fetuses with Down syndrome.
818 *Brain Pathol.* **28**, 986–998 (2018).
819 31. Holtzman, D. M., Santucci, D., Kilbridge, J., Chua-Couzens, J., Fontana, D. J., Daniels, S. E.,
820 *et al.* Developmental abnormalities and age-related neurodegeneration in a mouse
821 model of Down syndrome. *Proc. Natl. Acad. Sci. U. S. A.* **93**, 13333–13338 (1996).
822 32. Mori, T., Koyama, N., Arendash, G. W., Horikoshi-Sakuraba, Y., Tan, J. & Town, T.
823 Overexpression of human S100B exacerbates cerebral amyloidosis and gliosis in the
824 Tg2576 mouse model of Alzheimer's disease. *Glia* **58**, 300–314 (2010).
825 33. Trazzi, S., Fuchs, C., Valli, E., Perini, G., Bartesaghi, R. & Ciani, E. The amyloid precursor
826 protein (APP) triplicated gene impairs neuronal precursor differentiation and neurite
827 development through two different domains in the ts65dn mouse model for down
828 syndrome. *J. Biol. Chem.* **288**, 20817–20829 (2013).
829 34. Kurabayashi, N., Nguyen, M. D. & Sanada, K. DYRK1A overexpression enhances STAT
830 activity and astrogliogenesis in a Down syndrome mouse model. *EMBO Rep.* **16**, 1548–
831 1562 (2015).
832 35. Stagni, F., Giacomini, A., Emili, M., Uguagliati, B., Bonasoni, M. P., Bartesaghi, R., *et al.*
833 Subicular hypotrophy in fetuses with Down syndrome and in the Ts65Dn model of Down
834 syndrome. *Brain Pathol.* **29**, 366–379 (2019).
835 36. Lubiniecki, A. S., Blattner, W. A., Martin, G. M., Fialkow, P. J., Dosik, H., Eatherly, C., *et al.*
836 SV40 T-antigen expression in cultured fibroblasts from patients with Down syndrome and
837 their parents. *Am. J. Hum. Genet.* **31**, 469–477 (1979).
838 37. Laurent, L. C., Ulitsky, I., Slavin, I., Tran, H., Schork, A., Morey, R., *et al.* Dynamic changes
839 in the copy number of pluripotency and cell proliferation genes in human ESCs and iPSCs
840 during reprogramming and time in culture. *Cell Stem Cell* **8**, 106–118 (2011).
841 38. Taapken, S. M., Nisler, B. S., Newton, M. A., Sampsell-Barron, T. L., Leonhard, K. A.,
842 McIntire, E. M., *et al. Karotypic abnormalities in human induced pluripotent stem cells*
843 *and embryonic stem cells*. *Nature Biotechnology* vol. 29 313–314 (2011).
844 39. Papavassiliou, P., Charalsawadi, C., Rafferty, K. & Jackson-Cook, C. Mosaicism for trisomy
845 21: A review. *Am. J. Med. Genet. Part A* **167**, 26–39 (2015).
846 40. Weick, J. P., Held, D. L., Bonadurer, G. F., Doers, M. E., Liu, Y., Maguire, C., *et al.* Deficits
847 in human trisomy 21 iPSCs and neurons. *Proc. Natl. Acad. Sci. U. S. A.* **110**, 9962–7
848 (2013).

849 41. Hibaoui, Y., Grad, I., Letourneau, A., Sailani, M. R., Dahoun, S., Santoni, F. A., *et al.*
850 Modelling and rescuing neurodevelopmental defect of Down syndrome using induced
851 pluripotent stem cells from monozygotic twins discordant for trisomy 21. *EMBO Mol.*
852 *Med.* **6**, 259–77 (2014).
853 42. Murray, A., Letourneau, A., Canzonetta, C., Stathaki, E., Gimelli, S., Sloan-Bena, F., *et al.*
854 Brief Report: Isogenic Induced Pluripotent Stem Cell Lines From an Adult With Mosaic
855 Down Syndrome Model Accelerated Neuronal Ageing and Neurodegeneration. *Stem Cells*
856 **33**, 2077–2084 (2015).
857 43. MacLean, G. A., Menne, T. F., Guo, G., Sanchez, D. J., Park, I.-H., Daley, G. Q., *et al.*
858 Altered hematopoiesis in trisomy 21 as revealed through in vitro differentiation of
859 isogenic human pluripotent cells. *Proc. Natl. Acad. Sci.* **109**, 17567–17572 (2012).
860 44. Inoue, M., Kajiwara, K., Yamaguchi, A., Kiyono, T., Samura, O., Akutsu, H., *et al.*
861 Autonomous trisomic rescue of Down syndrome cells. *Lab. Investig.* **99**, 885–897 (2019).
862 45. Moullan, N., Mouchiroud, L., Wang, X., Ryu, D., Williams, E. G., Mottis, A., *et al.*
863 Tetracyclines disturb mitochondrial function across eukaryotic models: A call for caution
864 in biomedical research. *Cell Rep.* **10**, 1681–1691 (2015).
865 46. Izzo, A., Mollo, N., Nitti, M., Paladino, S., Calì, G., Genesio, R., *et al.* Mitochondrial
866 dysfunction in down syndrome: molecular mechanisms and therapeutic targets. *Mol.*
867 *Med.* **24**, 2 (2018).
868 47. Valenti, D., Braidy, N., De Rasmo, D., Signorile, A., Rossi, L., Atanasov, A. G., *et al.*
869 Mitochondria as pharmacological targets in Down syndrome. *Free Radic. Biol. Med.* **114**,
870 69–83 (2018).
871 48. Parra, V., Altamirano, F., Hernández-Fuentes, C. P., Tong, D., Kyrychenko, V., Rotter, D.,
872 *et al.* Down Syndrome Critical Region 1 Gene, Rcan1, Helps Maintain a More Fused
873 Mitochondrial Network. *Circ. Res.* **122**, e20–e33 (2018).
874 49. Wolvetang, E. ., Bradfield, O. ., Hatzistavrou, T., Crack, P. ., Busciglio, J., Kola, I., *et al.*
875 Overexpression of the chromosome 21 transcription factor Ets2 induces neuronal
876 apoptosis. *Neurobiol. Dis.* **14**, 349–356 (2003).
877 50. Hu, Y., Lehrach, H. & Janitz, M. Apoptosis screening of human chromosome 21 proteins
878 reveals novel cell death regulators. *Mol. Biol. Rep.* **37**, 3381–3387 (2010).
879 51. Noll, C., Tlili, A., Ripoll, C., Mallet, L., Paul, J. L., Delabar, J. M., *et al.* Dyrk1a activates
880 antioxidant NQO1 expression through an ERK1/2-Nrf2 dependent mechanism. *Mol.*
881 *Genet. Metab.* **105**, 484–488 (2012).
882 52. Liu, Y., Borel, C., Li, L., Müller, T., Williams, E. G., Germain, P. L., *et al.* Systematic
883 proteome and proteostasis profiling in human Trisomy 21 fibroblast cells. *Nat. Commun.*
884 *2017 81* **8**, 1–15 (2017).
885 53. Banda, E. & Grabel, L. Directed Differentiation of Human Embryonic Stem Cells into
886 Neural Progenitors. in *Methods in molecular biology (Clifton, N.J.)* vol. 1307 289–298
887 (2014).
888 54. Banda, E., McKinsey, A., Germain, N., Carter, J., Anderson, N. C. & Grabel, L. Cell Polarity
889 and Neurogenesis in Embryonic Stem Cell-Derived Neural Rosettes. *Stem Cells Dev.* **24**,
890 1022–1033 (2015).
891 55. Molofsky, A. V., Krencick, R., Ullian, E. M., Tsai, H. -h., Deneen, B., Richardson, W. D., *et*
892 *al.* Astrocytes and disease: a neurodevelopmental perspective. *Genes Dev.* **26**, 891–907

893 (2012).
894 56. Tobe, R., Naranjo-Suarez, S., Everley, R. A., Carlson, B. A., Turanov, A. A., Tsuji, P. A., *et al.*
895 High Error Rates in Selenocysteine Insertion in Mammalian Cells Treated with the
896 Antibiotic Doxycycline, Chloramphenicol, or Geneticin. *J. Biol. Chem.* **288**, 14709–14715
897 (2013).
898 57. Briggs, J. A., Sun, J., Shepherd, J., Ovchinnikov, D. A., Chung, T.-L., Nayler, S. P., *et al.*
899 Integration-Free Induced Pluripotent Stem Cells Model Genetic and Neural
900 Developmental Features of Down Syndrome Etiology. *Stem Cells* **31**, 467–478 (2013).
901 58. Beckervordersandforth, R. Mitochondrial Metabolism-Mediated Regulation of Adult
902 Neurogenesis. *Brain Plast.* **3**, 73–87 (2017).
903 59. Neri, F., Rapelli, S., Krepelova, A., Incarnato, D., Parlato, C., Basile, G., *et al.* Intragenic
904 DNA methylation prevents spurious transcription initiation. *Nat. 2017 5437643* **543**, 72–
905 77 (2017).
906 60. Wang, J., Syrett, C. M., Kramer, M. C., Basu, A., Atchison, M. L. & Anguera, M. C. Unusual
907 maintenance of X chromosome inactivation predisposes female lymphocytes for
908 increased expression from the inactive X. *Proc. Natl. Acad. Sci.* 201520113 (2016)
909 doi:10.1073/pnas.1520113113.
910 61. Chow, J. C., Hall, L. L., Baldry, S. E. L., Thorogood, N. P., Lawrence, J. B. & Brown, C. J.
911 Inducible XIST-dependent X-chromosome inactivation in human somatic cells is
912 reversible. *Proc. Natl. Acad. Sci. U. S. A.* **104**, 10104–9 (2007).
913 62. Kelsey, A. D., Yang, C., Leung, D., Minks, J., Dixon-McDougall, T., Baldry, S. E. L., *et al.*
914 Impact of flanking chromosomal sequences on localization and silencing by the human
915 non-coding RNA XIST. *Genome Biol.* **16**, 1–16 (2015).
916 63. Loda, A., Brandsma, J. H., Vassilev, I., Servant, N., Loos, F., Amirnasr, A., *et al.* Genetic and
917 epigenetic features direct differential efficiency of Xist-mediated silencing at X-
918 chromosomal and autosomal locations. *Nat. Commun. 2017 81* **8**, 1–16 (2017).
919 64. Wutz, A. Epigenetic Alterations in Human Pluripotent Stem Cells: A Tale of Two Cultures.
920 *Cell Stem Cell* **11**, 9–15 (2012).
921 65. Bansal, P., Ahern, D. T., Kondaveeti, Y., Qiu, C. W. & Pinter, S. F. Contiguous erosion of
922 the inactive X in human pluripotency concludes with global DNA hypomethylation. *Cell*
923 *Rep.* **35**, 109215 (2021).
924 66. Lois, C., Hong, E. J., Pease, S., Brown, E. J. & Baltimore, D. Germline transmission and
925 tissue-specific expression of transgenes delivered by lentiviral vectors. *Science* **295**, 868–
926 872 (2002).
927 67. DeKelver, R. C., Choi, V. M., Moehle, E. A., Paschon, D. E., Hockemeyer, D., Meijsing, S. H.,
928 *et al.* Functional genomics, proteomics, and regulatory DNA analysis in isogenic settings
929 using zinc finger nuclease-driven transgenesis into a safe harbor locus in the human
930 genome. *Genome Res.* **20**, 1133–42 (2010).
931 68. Liu, P., Jenkins, N. A. & Copeland, N. G. A Highly Efficient Recombineering-Based Method
932 for Generating Conditional Knockout Mutations. *Genome Res.* **13**, 476–484 (2003).
933 69. Chen, S. X., Osipovich, A. B., Ustione, A., Potter, L. A., Hipkens, S., Gangula, R., *et al.*
934 Quantification of factors influencing fluorescent protein expression using RMCE to
935 generate an allelic series in the ROSA26 locus in mice. *Dis. Model. Mech.* **4**, (2011).
936 70. Zhu, Z., González, F. & Huangfu, D. The iCRISPR Platform for Rapid Genome Editing in

937 Human Pluripotent Stem Cells. *Methods Enzymol.* **546**, 215–250 (2014).
938 71. Mcquin, C., Goodman, A., Chernyshev, V., Kamentsky, L., Cimini, A., Karhohs, K. W., *et al.*
939 Cellprofiler 3.0. *PLoS Biol.* 1–17 (2018).
940 72. Bushnell, B. BBTools.
941 73. Patro, R., Duggal, G., Love, M. I., Irizarry, R. A. & Kingsford, C. Salmon provides fast and
942 bias-aware quantification of transcript expression. *Nat. Methods* **14**, 417–419 (2017).
943 74. Love, M. I., Huber, W., Anders, S., Tusher, V., Banks, E., Fennell, T., *et al.* Moderated
944 estimation of fold change and dispersion for RNA-seq data with DESeq2. *Genome Biol.*
945 **15**, 550 (2014).
946 75. Wu, T., Hu, E., Xu, S., Chen, M., Guo, P., Dai, Z., *et al.* clusterProfiler 4.0: A universal
947 enrichment tool for interpreting omics data. *Innov.* **2**, 100141 (2021).
948 76. Aryee, M. J., Jaffe, A. E., Corrada-Bravo, H., Ladd-Acosta, C., Feinberg, A. P., Hansen, K. D.,
949 *et al.* Minfi: A flexible and comprehensive Bioconductor package for the analysis of
950 Infinium DNA methylation microarrays. *Bioinformatics* **30**, 1363–1369 (2014).
951 77. Kim, D., Paggi, J. M., Park, C., Bennett, C. & Salzberg, S. L. Graph-based genome
952 alignment and genotyping with HISAT2 and HISAT-genotype. *Nat. Biotechnol.* **37**, 907–
953 915 (2019).
954 78. Castel, S. E., Mohammadi, P., Chung, W. K., Shen, Y. & Lappalainen, T. Rare variant
955 phasing and haplotypic expression from RNA sequencing with phASER. *Nat. Commun.* **7**,
956 1–6 (2016).
957

Figure 1

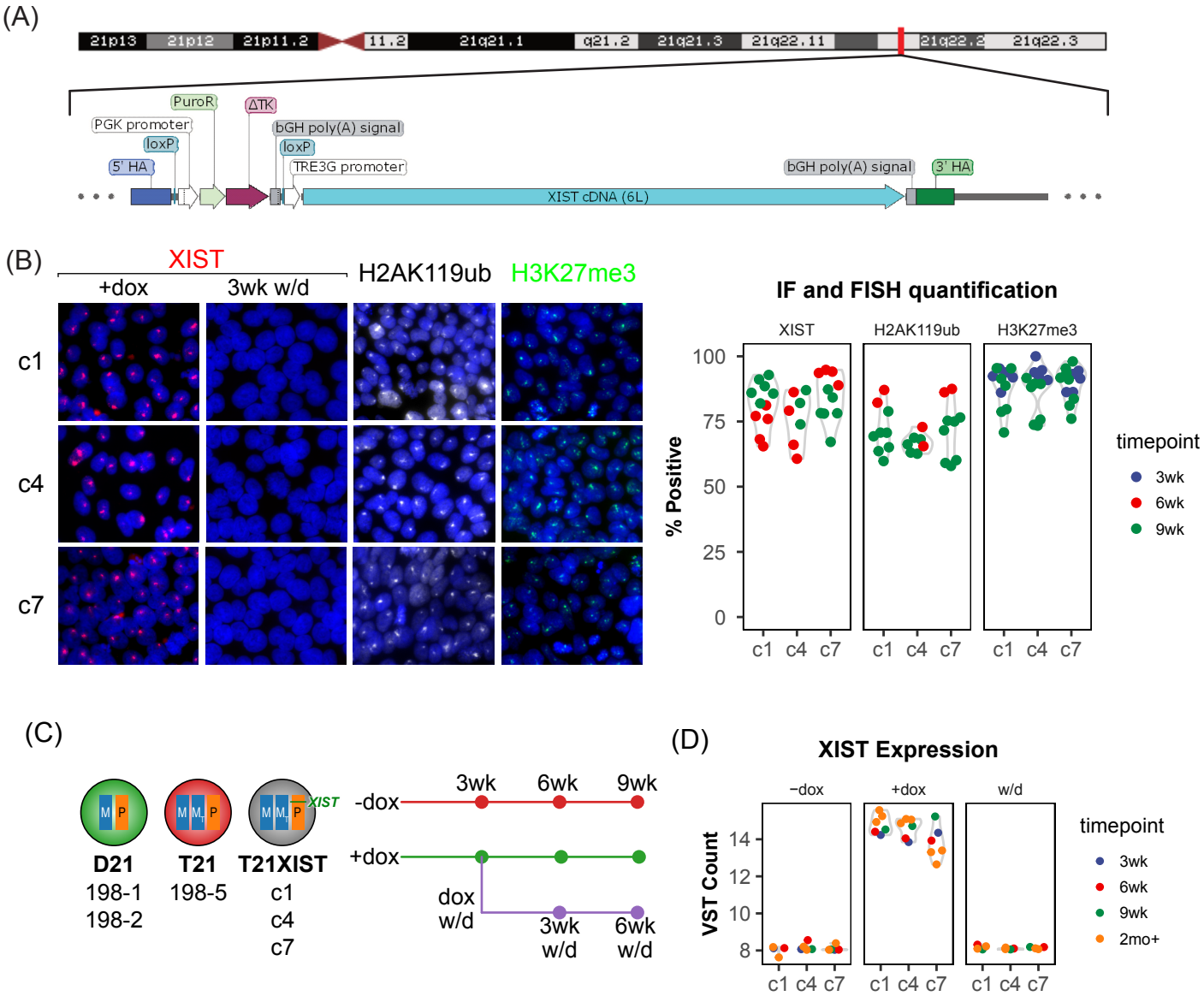
(A)
21p13
21p12
21p11.2
11.2
21q21.1
q21.2
21q21.3
21q22.11
21q22.2
21q22.3
PuroR
ΔTK
PGK promoter
bGH poly(A) signal
loxP
loxP
5' HA
TRE3G promoter
bGH poly(A) signal
3' HA
XIST cDNA (6L)
(B)
XIST
+dox
3wk w/d
H2AK119ub
H3K27me3
c1
c4
c7
IF and FISH quantification
XIST
H2AK119ub
H3K27me3
% Positive
100
75
50
25
0
c1 c4 c7
timepoint
3wk
6wk
9wk
(C)
M P
M M2 P
M M2 P
XIST
D21
198-1
198-2
T21
198-5
T21XIST
c1
c4
c7
-dox
+dox
3wk
6wk
9wk
dox w/d
3wk w/d
6wk w/d
(D)
XIST Expression
−dox
+dox
w/d
VST Count
14
12
10
8
c1 c4 c7
timepoint
3wk
6wk
9wk
2mo+

Figure 2

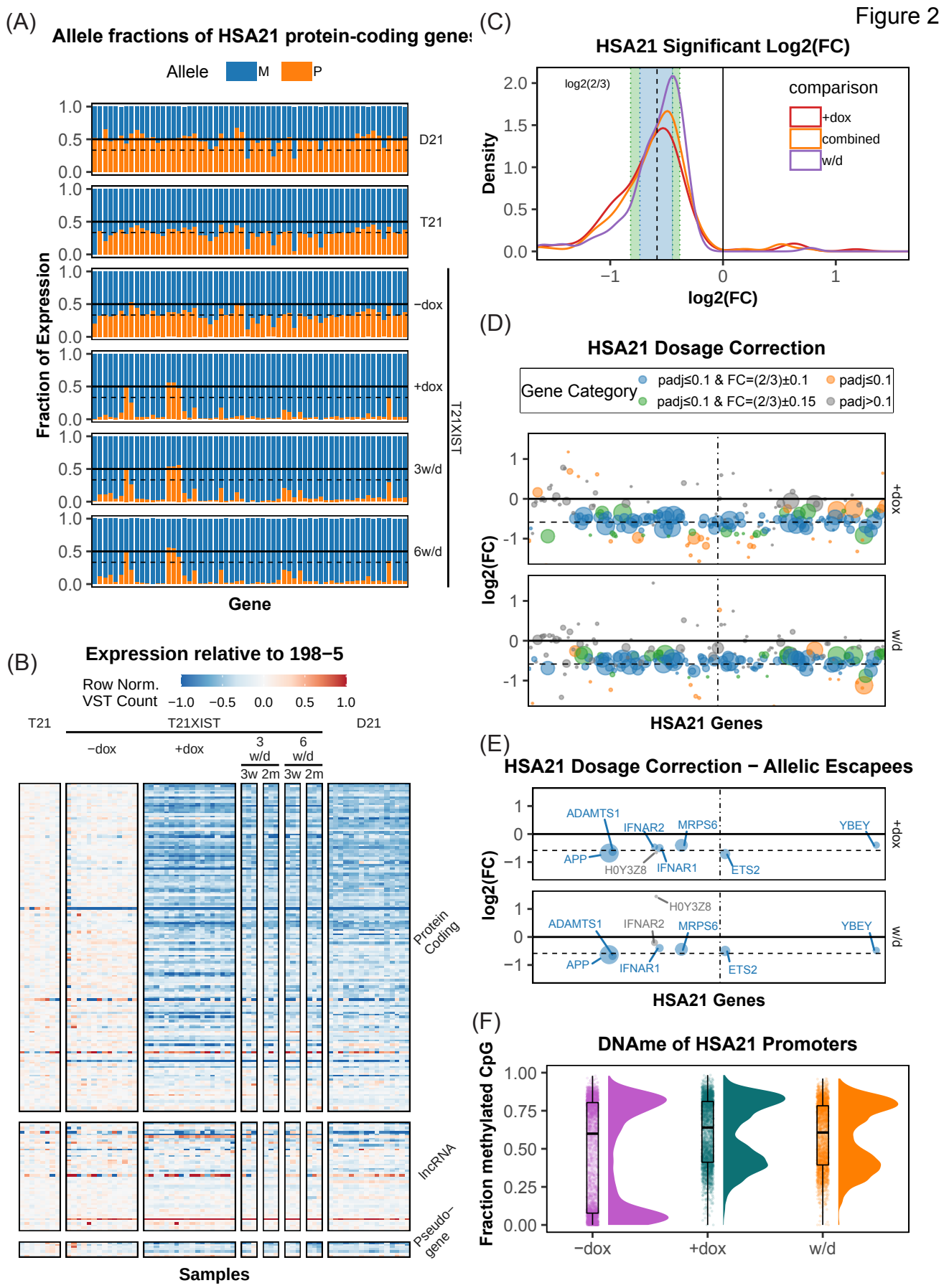
(A)
Allele fractions of HSA21 protein-coding genes
Allele
M
P
Fraction of Expression
D21
T21
−dox
+dox
3w/d
6w/d
T21XIST
Gene
(B)
Expression relative to 198−5
Row Norm.
VST Count
−1.0 −0.5 0.0 0.5 1.0
T21
T21XIST
D21
−dox
+dox
3 w/d
6 w/d
3w 2m 3w 2m
Protein Coding
lncRNA
Pseudo-gene
Samples
(C)
HSA21 Significant Log2(FC)
log2(2/3)
comparison
+dox
combined
w/d
Density
log2(FC)
(D)
HSA21 Dosage Correction
Gene Category
padj≤0.1 & FC=(2/3)±0.1
padj≤0.1
padj≤0.1 & FC=(2/3)±0.15
padj>0.1
log2(FC)
+dox
w/d
HSA21 Genes
(E)
HSA21 Dosage Correction − Allelic Escapees
ADAMTS1
IFNAR2
MRPS6
YBEY
APP
H0Y3Z8
IFNAR1
ETS2
log2(FC)
HSA21 Genes
(F)
DNAme of HSA21 Promoters
Fraction methylated CpG
−dox
+dox
w/d

Figure 3

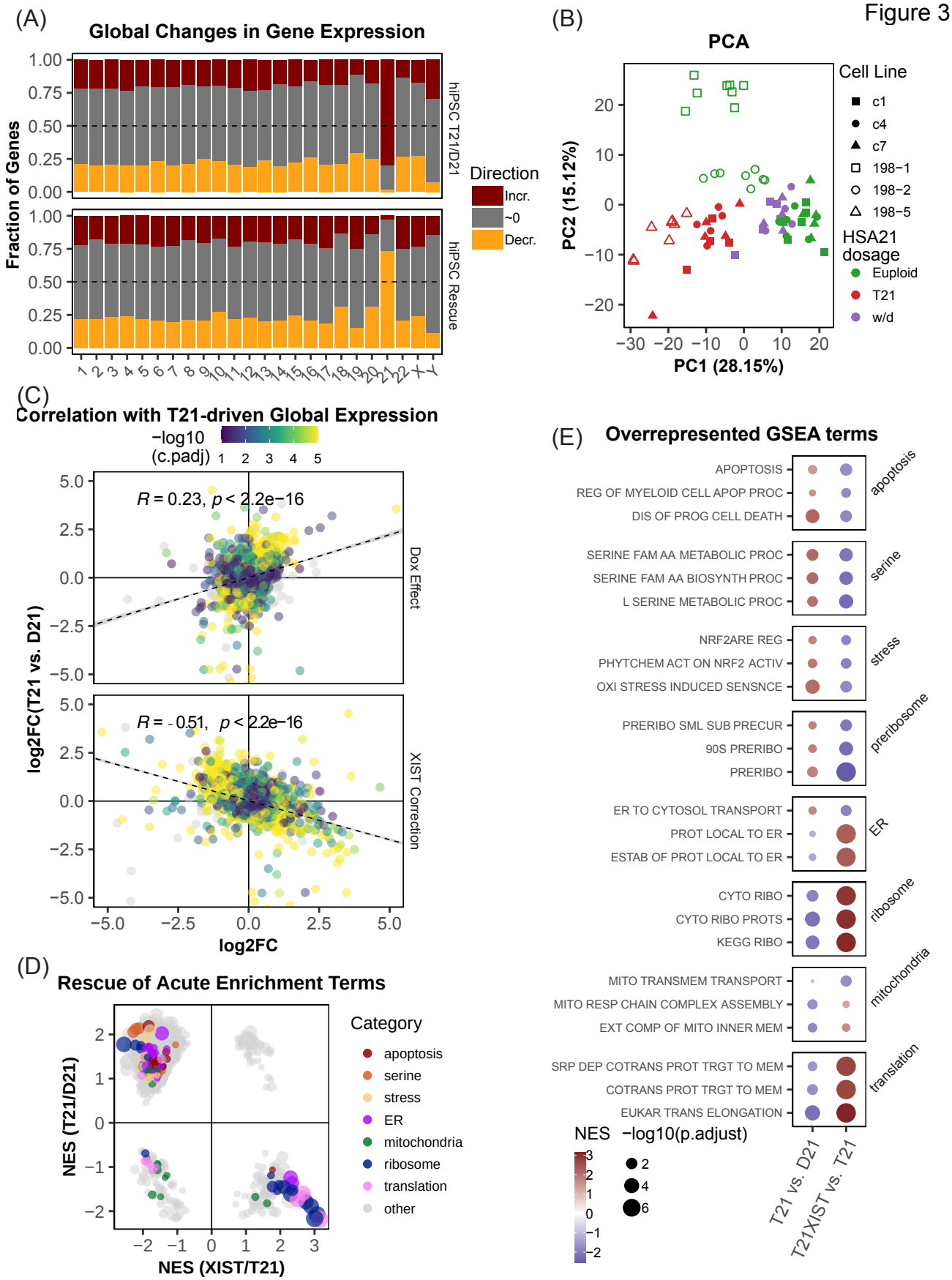
(A)
Global Changes in Gene Expression
Fraction of Genes
hiPSC T21/D21
hiPSC Rescue
Direction
Incr.
~0
Decr.
(B)
PCA
PC2 (15.12%)
PC1 (28.15%)
Cell Line
c1
c4
c7
198−1
198−2
198−5
HSA21 dosage
Euploid
T21
w/d
(C)
Correlation with T21-driven Global Expression
−log10 (c.padj)
R = 0.23, p < 2.2e−16
R = -0.51, p < 2.2e−16
Dox Effect
XIST Correction
log2FC(T21 vs. D21)
log2FC
(D)
Rescue of Acute Enrichment Terms
NES (T21/D21)
NES (XIST/T21)
Category
apoptosis
serine
stress
ER
mitochondria
ribosome
translation
other
(E)
Overrepresented GSEA terms
APOPTOSIS
REG OF MYELOID CELL APOP PROC
DIS OF PROG CELL DEATH
SERINE FAM AA METABOLIC PROC
SERINE FAM AA BIOSYNTH PROC
L SERINE METABOLIC PROC
NRF2ARE REG
PHYTCHEM ACT ON NRF2 ACTIV
OXI STRESS INDUCED SENSNCE
PRERIBO SML SUB PRECUR
90S PRERIBO
PRERIBO
ER TO CYTOSOL TRANSPORT
PROT LOCAL TO ER
ESTAB OF PROT LOCAL TO ER
CYTO RIBO
CYTO RIBO PROTS
KEGG RIBO
MITO TRANSMEM TRANSPORT
MITO RESP CHAIN COMPLEX ASSEMBLY
EXT COMP OF MITO INNER MEM
SRP DEP COTRANS PROT TRGT TO MEM
COTRANS PROT TRGT TO MEM
EUKAR TRANS ELONGATION
apoptosis
serine
stress
preribosome
ER
ribosome
mitochondria
translation
NES
−log10(p.adjust)
T21 vs. D21
T21XIST vs. T21

Figure 4

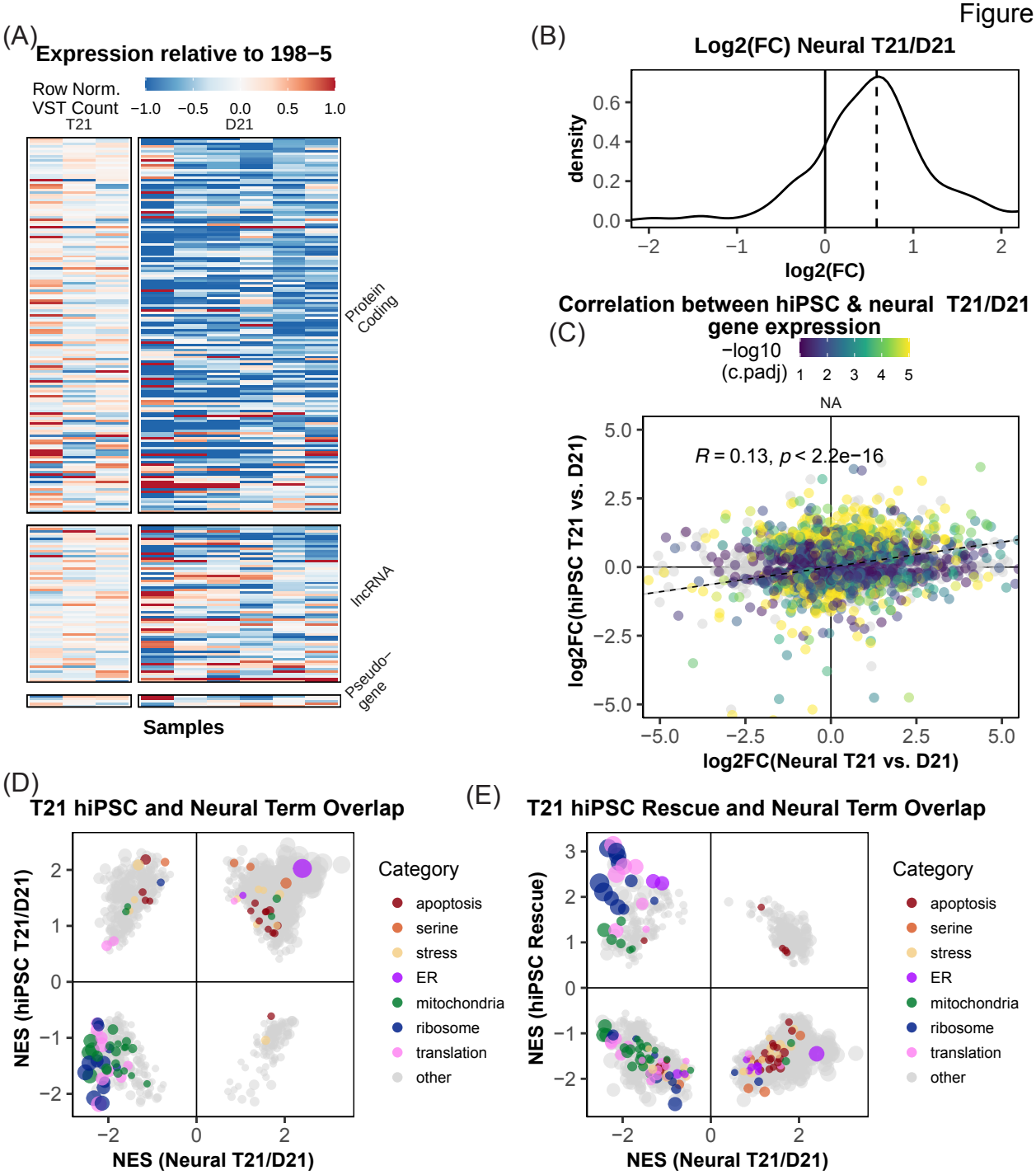
(A)
Expression relative to 198−5
Row Norm.
VST Count
−1.0 −0.5 0.0 0.5 1.0
T21
D21
Protein Coding
lncRNA
Pseudo-gene
Samples
(B)
Log2(FC) Neural T21/D21
density
log2(FC)
(C)
Correlation between hiPSC & neural T21/D21 gene expression
−log10 (c.padj)
1 2 3 4 5
NA
R = 0.13, p < 2.2e−16
log2FC(hiPSC T21 vs. D21)
log2FC(Neural T21 vs. D21)
(D)
T21 hiPSC and Neural Term Overlap
NES (hiPSC T21/D21)
NES (Neural T21/D21)
Category
apoptosis
serine
stress
ER
mitochondria
ribosome
translation
other
(E)
T21 hiPSC Rescue and Neural Term Overlap
NES (hiPSC Rescue)
NES (Neural T21/D21)
Category
apoptosis
serine
stress
ER
mitochondria
ribosome
translation
other

Figure 5

(A)

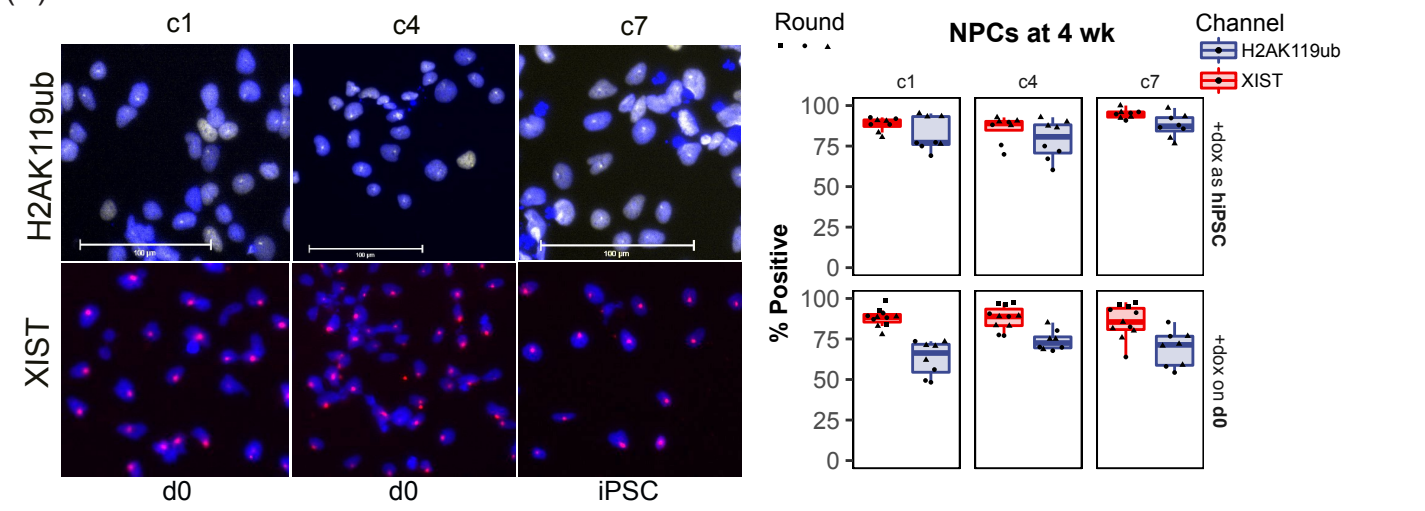
c1
c4
c7
H2AK119ub
XIST
d0
d0
iPSC
Round
NPCs at 4 wk
Channel
H2AK119ub
XIST
% Positive
+dox as hiPSC
+dox on d0

(B)

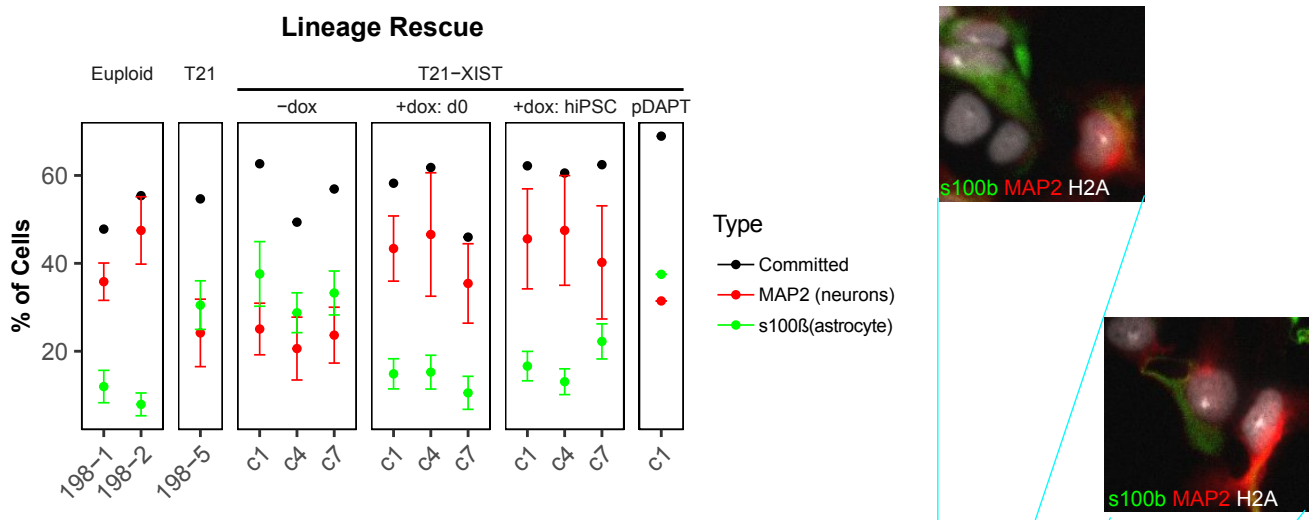
Lineage Rescue
Euploid
T21
T21−XIST
−dox
+dox: d0
+dox: hiPSC
pDAPT
% of Cells
198−1
198−2
198−5
c1
c4
c7
Type
Committed
MAP2 (neurons)
s100ß(astrocyte)
s100b MAP2 H2A
s100b MAP2 H2A

(C)

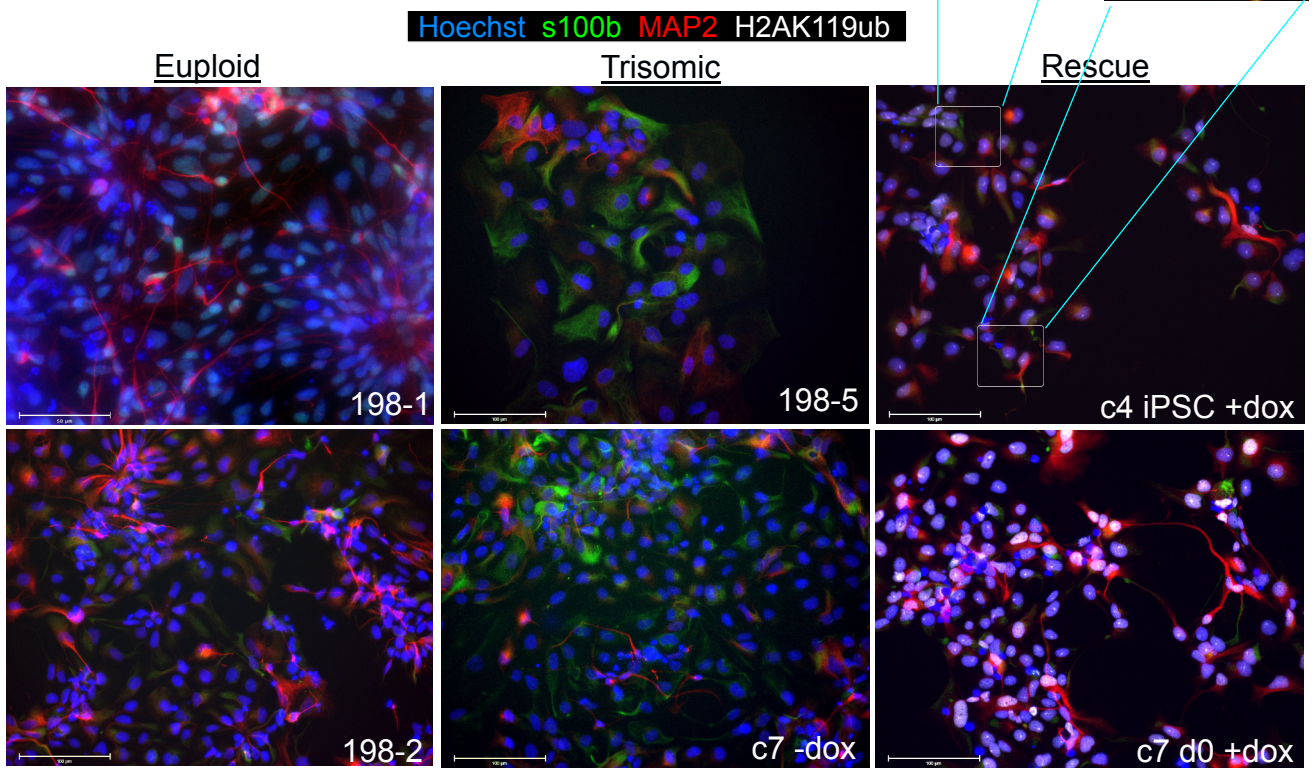
Hoechst s100b MAP2 H2AK119ub
Euploid
Trisomic
Rescue
198-1
198-5
c4 iPSC +dox
198-2
c7 -dox
c7 d0 +dox

Figure 6

(A)

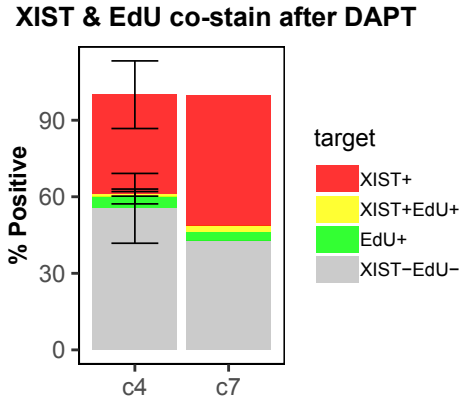
XIST & EdU co-stain after DAPT
% Positive
90
60
30
0
c4
c7
target
XIST+
XIST+EdU+
EdU+
XIST−EdU−

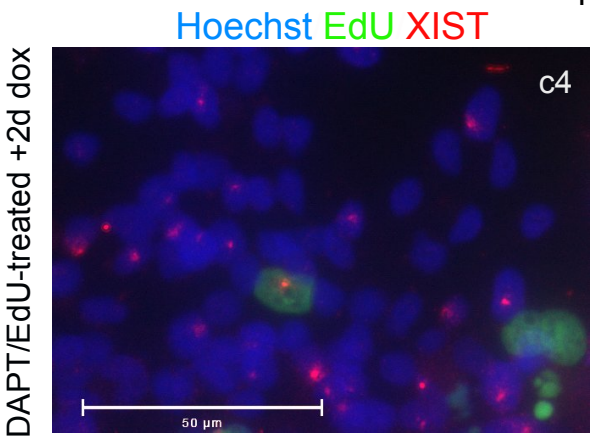
Hoechst EdU XIST
DAPT/EdU-treated +2d dox
c4
50 µm

(B)

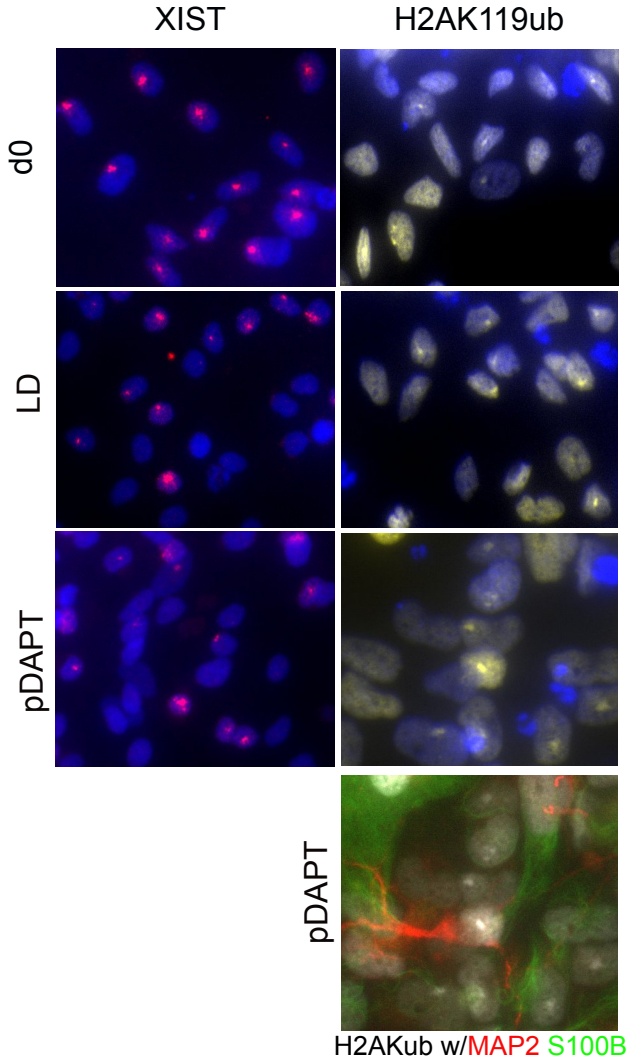
XIST
H2AK119ub
d0
LD
pDAPT
pDAPT
H2AKub w/MAP2 S100B

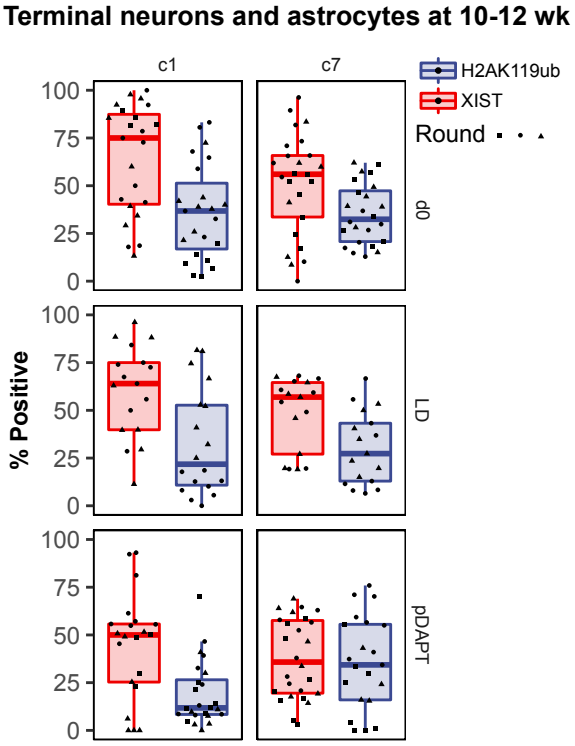
Terminal neurons and astrocytes at 10-12 wk
c1
c7
H2AK119ub
XIST
Round
% Positive
100
75
50
25
0
d0
LD
pDAPT